



Deposited via The University of York.

White Rose Research Online URL for this paper:

<https://eprints.whiterose.ac.uk/id/eprint/180566/>

Version: Accepted Version

---

**Article:**

Al-Mikhlaifi, Ahmed Saif, Hibbert, Fiona D., Edwards, Lawrence R. et al. (2021) Holocene relative sea-level changes and coastal evolution along the coastlines of Kamaran Island and As-Salif Peninsula, Yemen, southern Red Sea. *Quaternary Science Reviews*. 106719. ISSN: 0277-3791

<https://doi.org/10.1016/j.quascirev.2020.106719>

---

**Reuse**

This article is distributed under the terms of the Creative Commons Attribution-NonCommercial-NoDerivs (CC BY-NC-ND) licence. This licence only allows you to download this work and share it with others as long as you credit the authors, but you can't change the article in any way or use it commercially. More information and the full terms of the licence here: <https://creativecommons.org/licenses/>

**Takedown**

If you consider content in White Rose Research Online to be in breach of UK law, please notify us by emailing [eprints@whiterose.ac.uk](mailto:eprints@whiterose.ac.uk) including the URL of the record and the reason for the withdrawal request.

1 **Holocene relative sea-level changes and coastal evolution along the coastlines of**  
2 **Kamaran Island and As-Salif Peninsula, Yemen, southern Red Sea**

3 Ahmed Saif Al-Mikhlaifi<sup>(1)</sup>, Fiona D. Hibbert<sup>(2)</sup>, Lawrence R. Edwards<sup>(3)</sup>, Hai Cheng<sup>(3)</sup>

4

5 (1) Department of Earth and Environmental Sciences, Sana'a University, Sana'a,  
6 Republic of Yemen

7 (2) Research School of Earth Sciences, The Australian National University, Canberra,  
8 ACT 2601, Australia

9 (3) Department of Earth Sciences, University of Minnesota, Minneapolis, MN 55455.  
10 USA.

11

12 Corresponding author: Ahmed Saif Al-Mikhlaifi ([ahmed.almikhlaifi@fulbrightmail.org](mailto:ahmed.almikhlaifi@fulbrightmail.org);  
13 [ahmedmikhlaifi@hotmail.com](mailto:ahmedmikhlaifi@hotmail.com))

14

15 **Abstract**

16 Geomorphic features (fossil terraces, notches and sea cliffs) from the southern Red  
17 Sea coasts provide valuable indicators of past sea-level change that enable the  
18 quantification of both the timing and magnitude of the mid-Holocene sea-level  
19 highstand. We demonstrate the utility of wave-cut notches in the southern Red Sea,  
20 and present U-series dated sea-level indicators from two locations on the As-Salif  
21 Peninsula that suggest a mid-Holocene highstand of ~ 0.5 to 1 m above present  
22 mean sea level (apmsl) at about 5 to 5.4 ka BP. In addition, the similarity of the  
23 elevations of the different sea-level indicators at the two locations in As-Salif  
24 Peninsula and Kamran Island suggest relative tectonic stability, with limited influence  
25 of salt diapirism. Comparison of our data to other estimates of the Red Sea mid-  
26 Holocene highstand, and glacio-isostatic predictions suggest that water loading (and  
27 deformational response) is the primary factor in the spatial and temporal variability  
28 the mid-Holocene highstand, with some possible localized tectonic and neotectonic  
29 overprinting.

30

31 **Key words:**

32 Red Sea; mid-Holocene sea level; coastal geomorphology; fossil corals; wave-cut

33 notches; U-series dating

34

## 35 **1. INTRODUCTION**

36 Relatively little is known about the relative sea level (RSL) variations during the  
37 Holocene for large segments of the Red Sea coasts, especially the south of the basin  
38 (e.g., [Edelman-Furstenberg et al., 2001](#); [Lamy et al., 2006](#); [Lambeck et al., 2011](#)).

39 Early studies assigned emerged sea-level indicators (e.g., coral terraces) along the  
40 Red Sea coast to sea-level fluctuations and tectonic processes only, and ignored  
41 contributions from the glacio-isostatic adjustment (GIA) and water loading processes  
42 (e.g., [Al-Rifaiy and Cherif, 1988](#); [Gvirtzman et al., 1992](#); [El-Asmar, 1997](#); [Strasser and](#)  
43 [Strohenger, 1997](#); [Shaked et al., 2002](#)). As GIA affects not just near-field regions  
44 (i.e., those located close to the former ice sheets) but also the intermediate and  
45 locations such as the Red Sea ([Mitrovica and Peltier, 1991](#); [Peltier, 1999](#); [Milne and](#)  
46 [Mitrovica, 2008](#); [Lambeck et al., 2014](#)), considerable spatial variability in amplitude,  
47 magnitude and timing of highstands in the Red Sea is expected and predicted from  
48 GIA modelling ([Lambeck et al., 2011](#)).

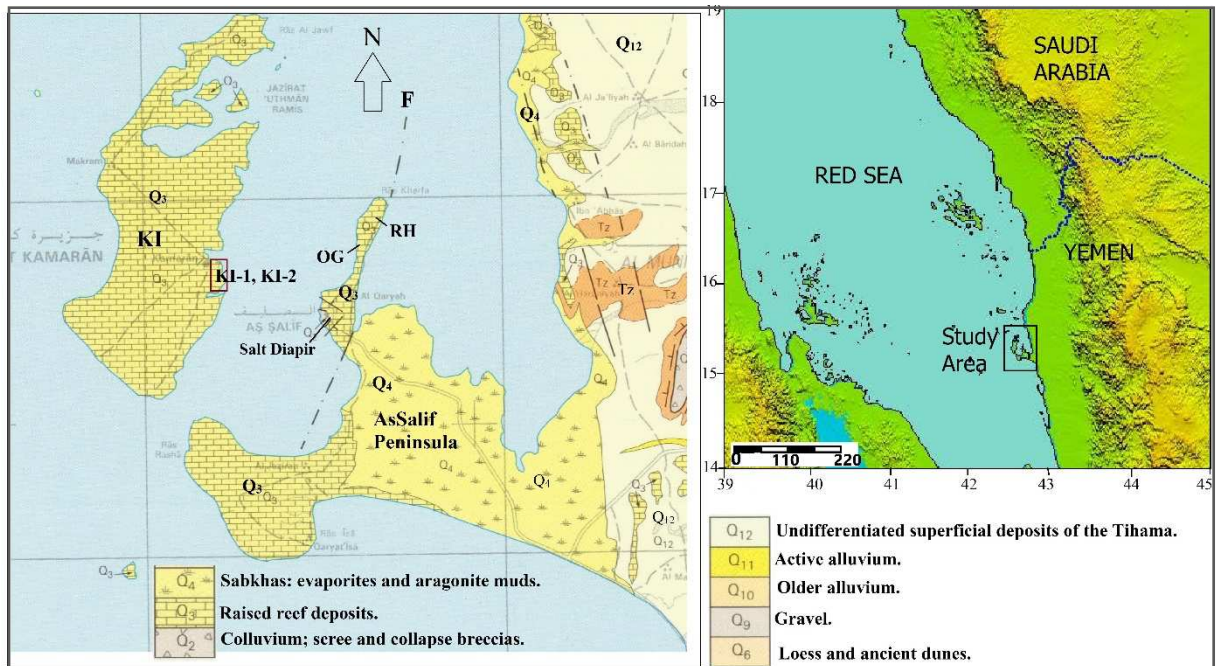
49

50 Tectonically, the Red Sea is not stable and geologic, geodetic and seismic evidence  
51 indicates pronounced vertical movements across the Red Sea basin throughout the  
52 latest rifting phase that started in the Miocene ([Girdler and Styles, 1974](#); [Hötzl, 1984](#);  
53 [Hempton, 1987](#); [Purser and Bosence, 1998](#)). In addition, vertical movement  
54 associated salt diapirism occurs in some parts of the Red Sea, such as the As-Salif  
55 Peninsula ([Figure 1](#)) and these vertical movements have influenced the carbonate  
56 reef deposits, often resulting in irregular uplift of the terraces.

57

58 As indicators of local sea level form as a result of the interplay between eustatic sea-  
59 level change, tectonic uplift or downwarping, and GIA processes, we expect the  
60 combined imprint of each of these processes to be preserved at the stratigraphic  
61 record of the Red Sea. In this study we utilize wave-cut notches from the southern  
62 Red Sea, Kamaran Island and the As-Salif Peninsula, to provide information on both  
63 local tectonic history and past sea level. We provide mid-Holocene coral U-series  
64 ages for the Yemeni Red Sea coast and document geomorphic features on As-Salif

65 Peninsula and Kamaran Island coasts. We take advantage of the varied geologic/  
 66 neotectonic setting of the area to: (i) investigate the potential of wave-cut notches  
 67 as a palaeo tide and sea-level indicators in the Red Sea; (ii) provide sea-level  
 68 constraints to test the GIA predictions of Red Sea sea levels during the Holocene;  
 69 and (iii) interpret the tectonic history of the complex, faulted region in the southern  
 70 Red Sea.  
 71



72  
 73 **Figure 1:** Topographic map of Yemeni Red Sea showing Kamaran and As-Salif  
 74 Peninsula and the study/sampling locations (OM = Om Gedi; RH = Ras Harafa; KI-1  
 75 and KI-2 are the two sampling locations on Kamaran Island).

76

77 **2. LOCATION, GEOMORPHOLOGY AND STRATIGRAPHY**

78

79 **2.1 Tidal regime and coastal setting**

80 The Red Sea is characterized by a semi-diurnal microtidal regime, with the tidal  
 81 range increasing with distance from the centre of the basin, from virtually no daily  
 82 change to about 0.6 m in the north and up to 0.9 m in the south (at Massawa and  
 83 Kamaran Island) (Edwards, 1987). The tidal range results from the interaction of  
 84 tides produced in the Red Sea itself and the co-oscillation with the Indian Ocean  
 85 (Defant, 1961). The latter is attenuated by the narrow Bab al Mandeb Strait resulting

86 in generally low tidal amplitudes in the Red Sea. The effect of the strait can be seen  
87 from increasing tidal amplitudes northwards, with the highest tidal range recorded  
88 in Kamaran Island of ~ 1 m.

89

90 The wave regime (direction, wave height) at the study sites is driven by three  
91 principal seasonal wind systems operating in the Red Sea, and waves tend to  
92 propagate along the axis of the Red Sea basin (Clifford et al., 1997; Sofianose, 2003;  
93 Langodan et al., 2017). Significant wave height varies seasonally with the monsoon  
94 reversal (Ralston et al., 2013; Langodan et al., 2018); during the winter, monsoon  
95 winds from the southeast generate waves with mean significant wave heights in  
96 excess of 2 m and mean periods of 8 s in the southern Red Sea, with lower wave  
97 heights during the summer (Ralston et al., 2013). The indented coasts of the Red Sea  
98 leads to a reduction in swell, especially in the southern zone (Langodan et al., 2017).

99

## 100 **2.2 As-Salif Peninsula**

101 The As-Salif Peninsula is part of the ~40 km wide, N-S trending, Tihama coastal plain  
102 (Davison et al., 1994) (Figure1). The southern Red Sea, including islands and volcanic  
103 coastal formations, are associated with the main Red Sea Rift and Afar rift, which are  
104 parallel to the coast and have numerous fault lines (Rowlands and Purkis, 2015). An  
105 irregular distribution of carbonate bodies occurs as a result of local faults,  
106 differential uplift due to salt diapirs, and variable erosion/depositional processes  
107 (Bosence, 2005; Purkis et al., 2012; Rowlands and Purkis, 2015). Tectonically, the As-  
108 Salif Peninsula is an intensely deformed area, with vertical bedding and steeply  
109 plunging isoclinal folds (Davison et al., 1996).

110

111 The geomorphology of Red Sea makes it conducive to evaporite and salt diapir  
112 formation (Bosworth, 2015) with mid- to late Miocene salt deposits (16.4-5.3 Ma)  
113 forming shortly after Red Sea basin rifting terminated (Heaton et al., 1996; Davison  
114 et al., 1996). The vast desert and arid climate of the region also create the conditions  
115 for salt diapirs to form and develop into domes and islands (Bosence, 2005). The  
116 evaporites in this region are sandwiched between Pliocene siliciclastics sediments

117 beneath, and Pleistocene and Holocene carbonates above ([Brown, 1970](#); [Mitchell et](#)  
118 [al., 1992](#); [Bosence et al., 1998](#)). The stress exerted by the rocks above, force the  
119 evaporites to elevate the overlaying strata to create diapiric structures ([Purser and](#)  
120 [Bosence, 1998](#); [Bosence et al., 1998](#); [Gracia et al., 2008](#)).

121

122 The As-Salif Peninsula is produced by a linear north-south trending salt diapir,  
123 bounded by a normal growth fault on the eastern margin, and this diapiric wall  
124 continues offshore for several kilometres ([Bosence et al., 1998](#)). Boreholes drilled in  
125 the region show that evaporite influence is unevenly distributed beneath the coastal  
126 shelf, and the thickest evaporites are found offshore ([Bosence et al., 1998](#); [Rowlands](#)  
127 [et al., 2014](#)). The domed morphology of As-Salif diapir is topped by corals dominated  
128 by *Galaxea fascicularis*, particularly in the lower sections of the fossil reefs, with  
129 more diverse coral assemblage in the upper section of the reefs ([Bosence, 2005](#);  
130 [Purkis and Riegl, 2012](#)) ([Figure 2](#)).

131

132 In brief, the Salif Formation in the region comprises a thick halite, disconformably  
133 overlain by bedded gypsum with thin layers of carbonate (the Ghawwas Member),  
134 capped by about 5 m of gypsiferous/calcareous clastics. The Salif Formation is  
135 intermittently exposed along the coastal region of the Tihamah plain of the Yemeni  
136 Red Sea and we selected two emergent terraces for further investigation. These  
137 comprise two low lying, flat-topped emergent terraces in the northern As-Salif  
138 Peninsula, Om Gedi and Ras Harafa ([Figure 1](#)). A normal fault, which is oriented  
139 parallel to salt diapir faults, passes through the northernmost As-Salif Peninsula, and  
140 may be responsible for the emergence of these terraces ([Rowlands and Purkis,](#)  
141 [2015](#)).

142

143 The Om Gedi terrace (OG) (upper Salif Formation), is formed predominantly of  
144 coarse to fine grained siliciclastic lithology impregnated with gypsiferous/anhydrite  
145 beds ([Figure 3](#)). Such deposits are typically a result of sabkha cycles, where  
146 alternating episodes of sea water saturation and flushing with meteoric water in  
147 intertidal sediments lead to gypsum formation ([Wright, 1994](#)). The high content of  
148 siliciclastic grains suggests deposition by wind ([Youssef, 1991](#)).

149

150 The Ras Harafa terrace (RH) is largely formed of gypsum and gypsiferous clastics  
151 intercalated with detrital material (also upper Salif Formation) (El-Nakhal and Alaug,  
152 2013; Beydoun et al., 1998), with a series of cliffs, notches, and caves on its seaward  
153 face. Recent gypsum deposits encrust coral reef fragments atop a wave-cut platform  
154 below to marine terrace (Figure 4). The shape and location of the As-Salif Peninsula  
155 terraces suggests a primary tectonic control on their spatial distribution.

156

### 157 **2.3. Kamaran Island**

158 Kamaran Island (KI) is located in shallow waters of north-eastern part of Yemeni Red  
159 Sea and separated from the eastern coast by a narrow strait known as As-Salif strait  
160 (Figure 1). The island is a post-rift sequence formed of carbonate deposits that  
161 developed on the eroded uppermost layer of the Plio-Pleistocene platform  
162 (Angelucci, 1981; Angelucci et al., 1985). These carbonate deposits (reefal  
163 limestones, ca. 1.81 - 0.01 Ma) represent the uppermost 10 m of a shallow water  
164 sedimentary complex that overlies an evaporite sequence of Miocene age (Davison  
165 et al., 1996; Bosence et al., 1998).

166

167 A sequence of notches, cliffs, and platforms is evident in the carbonate rocks of  
168 Kamaran Island. These were incised through tidal and/or wave action and can be  
169 used as a palaeo-sea level indicators, although debate as to the exact processes  
170 governing formation continues (e.g., Pirazzoli, 1986; Rust and Kershaw, 2000;  
171 Kershaw and Guo, 2001; Kelletat, 2005; Evelpidou et al., 2012; Moses, 2013). Recent  
172 sediments comprise mostly of fossil remains (e.g., corals, molluscs, calcareous algae,  
173 and benthic foraminifera) and reworked materials from the nearby rocks.

174

## 175 **3. MATERIALS AND METHODS**

176 We mapped the geomorphic features (wave-cut notches, cliffs etc.) at each site;  
177 elevations were determined using either direct measurement by levelling and/or  
178 differential Global Positioning System (GPS) measurements and are reported relative  
179 to present mean sea level (above present mean sea level, apmsl). The uncertainty in  
180 the GPS elevation measurement is  $\pm 2$  cm, with greater uncertainty associated with

181 our levelling (we use a conservative estimate of 20 %). The inflection points of wave-  
182 cut notches indicates the position of mean sea level at the time of formation  
183 ([Antonioli et al., 2015](#)). However, we had difficulty in determining the vertex at our  
184 sites, as most of the notches are of U-shape and/or obscured by sediment. As such,  
185 we report the approximate elevation of the inflection point through comparison  
186 with analogue modern notches. The total elevation error was calculated by summing  
187 all the contributing sources of error in quadrature ([Table 1](#)).

188

189 We collected *in situ* *Porites* sp. and *Acropora* sp. corals (i.e., the corals were found  
190 upright in growth position, with no indication of later displacement) for U-series  
191 dating. We assume corals from the fossil reef platform immediately below the wave-  
192 cut notches lived at the time as when the notch was cut (cf. [Rovere et al., 2015](#);  
193 [Lorscheid et al., 2017](#)). Modern corals in the area are intertidal. Twelve coral samples  
194 were collected ([Table 1](#)): 6 samples from two locations in Kamran Island (KI01 and  
195 KI02) (at  $+4 \pm 1$  m apmsl), two *in situ* corals from a patch reef on top of the As-Salif  
196 diapirs ( $+18 \pm 2$  m apmsl); two *in situ* corals from the Om Gedi (OG) ( $+1 \pm 0.2$  m  
197 apmsl) and; two corals *in growth* position from Ras Harafa (RH) ( $+0.5 \pm 0.2$  m apmsl)  
198 ([Figure 1](#)).

199

200 Corals selected for radiometric dating were initially examined petrographically and  
201 by X-ray diffraction to ensure that corals were primary aragonite. The XRD  
202 determinations were carried out using Rigaku Miniflex XRD, with JADE 7 software  
203 ([Connolly, 2010](#)) used for peak identification. All corals collected from the As-Salif  
204 peninsula terraces are pristine (i.e.,  $< 2$  % calcite), whereas the coral samples from  
205 Kamaran Island were diagenetically altered (i.e., recrystallized) and only two samples  
206 from Kamaran Islands with the least amount of alteration (visual appearance and %  
207 calcite) were U-series dated. Samples that passed the initial XRD screening were  
208 lightly crushed and any discoloured material and/or debris was removed using a  
209 binocular microscope. Coral samples were then quarried out into cubes followed by  
210 multiple ultrasonic baths in distilled water, and dried at 30°C. The chemical  
211 procedures for the separation of U and Th from the sample are based on methods of  
212 [Edwards et al. \(1987\)](#). Approximately 0.2 - 0.3 g of ultrasonically cleaned samples

213 were weighed and spiked with a mixed  $^{229}\text{Th}$ - $^{233}\text{U}$ - $^{236}\text{U}$  tracer. Uranium and thorium  
214 were separated with iron co-precipitation and anion-exchange chromatography. The  
215 uranium and thorium aliquots were dissolved in 1%  $\text{HNO}_3$  + 0.005N HF for  
216 instrumental measurements (Shen et al., 2002). Samples were subsequently  
217 analyzed by Neptune multi-collector inductively coupled plasma mass spectrometer  
218 (MC-ICP-MS) and a Faraday-multiplier following the procedure developed by  
219 Edwards et al. (1987, 1988); Cheng et al. (2008) and Shen et al. (2002). Ages were  
220 calculated using a half-life for  $^{230}\text{Th}$  of 75,690 years and a half-life for  $^{234}\text{U}$  of 245,250  
221 years (Cheng et al., 2013). The age was solved for iteratively using the standard age  
222 equation presented in Edwards et al. (1987), using decay constants of  $1.55125 \times 10^{-10}$   
223 for  $\lambda_{238}$  (Jaffey et al., 1971),  $2.82206 \times 10^{-6}$  for  $\lambda_{234}$  (Cheng et al., 2013), and  $9.1705$   
224  $\times 10^{-6}$  for  $\lambda_{230}$  (Cheng et al., 2013). In addition, samples were corrected for initial non-  
225 radiogenic thorium using a  $^{230}\text{Th}/^{232}\text{Th}$  atomic ratio of  $4.4 \pm 2.2 \times 10^{-6}$ .

226

## 227 4. RESULTS

### 228 4.1 U-series dating

229 Five *in situ* coral samples were collected from As-Salif Peninsula (two from the top of  
230 As-Salif Salt diapir, two from Ras Harafa (RH), and one from Om Gedi (OG). The  
231 measured  $^{238}\text{U}$  concentrations of our samples varies between 1.14 and 2.61 ppm  
232 (Table 1). Samples from RH have  $^{238}\text{U}$  concentrations consistent to modern pristine  
233 corals of living/dead corals from Bab al-Mandab (Al-Mikhlafi et al., 2018), and  
234 modern corals from Red Sea (Friedman, 1968; Gvirtzman et al., 1973). However,  
235 Holocene corals from the Om Gedi and As-Salif salt diapir have lower  $^{238}\text{U}$   
236 concentrations (Table 1), suggesting that these corals may have experienced  
237 secondary elemental or isotopic disturbance (cf. Yu and Zhao, 2010). The  
238 concentration of  $^{232}\text{Th}$  in our samples varies from  $0.375 \pm 0.009$  to  $1.59 \pm 0.033$  ppb,  
239 the latter is significantly above the 0.5 ppb of pristine corals from oceanic islands and  
240 likely reflects the incorporation of detrital material into the corals (Edwards et al.,  
241 1987; Chen et al., 1991; Yokoyama et al., 2001). The modern value of  $\delta^{234}\text{U}_i$  is widely  
242 used to detect diagenetic alteration of fossil corals (e.g., Bard et al., 1991; Hamelin et  
243 al., 1991; Gallup et al., 1994) and all samples except those from Kamaran Island have  
244 calculated  $\delta^{234}\text{U}_i$  values that are similar to the modern seawater value ( $146.8 \pm 1$  ‰,

245 Andersen et al., 2010).

246

**Table 1.** U-series data of samples from Kamaran Island and As-Salif peninsula, southern Red Sea. All uncertainties are reported at the 2 sigma uncertainty level.

Sample/ Species	Elev. (m)	<sup>238</sup> U (ppm)	<sup>232</sup> Th (ppb)	<sup>230</sup> Th/ <sup>232</sup> Th (atomic x10 <sup>-6</sup> )	δ <sup>234</sup> U* (meas.)	<sup>230</sup> Th/ <sup>238</sup> U (activity)	<sup>230</sup> Th Age (yr) (uncorrected)	<sup>230</sup> Th Age (yr) (corrected)	δ <sup>234</sup> U <sub>initial</sub> ** (corrected)	<sup>230</sup> Age (yr BP)*** (corrected)
<b>Bab El-Mandab: Living or modern-dead corals collected from ~2 m b.s.l near to Perim Island (AL-Mikhlafi et al., 2018).</b>										
BM01 <i>Porites</i> sp.	-2±0.5	2.14 ±0.002	0.0401±0.004	78.4±93.9	146.4±1.2	0.0001±0.0001	8±10	8±10	146 ±1	-53±10
BM02 <sup>§</sup> <i>D. strigosa</i>	-2±0.5	2.72 ±0.003	0.1827±0.005	28.8±20.5	146.9±1.3	0.0001±0.0001	11±8	9±80	147±1	-52±80
BM03 <i>Porites</i> sp.	-2±0.5	2.09 ±0.003	0.8469±0.018	13.8±3.3	144.5±1.5	0.0003±0.0001	32±8	22±11	145±2	-41±11
<i>Note: BM 01 and 02 are different samples (new collections), BM 03 is from different location (old collections)</i>										
<b>As Salif (Holocene corals)</b>										
OG01 <i>Porites</i> sp.	1.0±0.2	1.21±0.0015	1.42±0.0291	727.9±15.1	144.2±1.5	0.0518±0.0002	5043±21	5013±30	146±2	4950±30
RH01 <i>Acropora</i> sp.	0.5±0.2	2.61±0.005	1.5865±0.0333	1528.0±34.1	142.1±2.5	0.0562±0.0004	5500±46	5485±47	144±3	5423±47
RH02 <i>Acropora</i> sp.	0.5±0.2	2.48±0.0049	0.8766±0.0185	2575.9±55.2	143.6±2.1	0.0553±0.0002	5395±24	5386±25	146±2	5324±25
SL01 <i>Porites</i> sp.	18±2	1.42±0.0019	0.3749±0.0092	4866.0±120.4	147.3±1.8	0.0782±0.0002	7685±26	7679±26	150±2	7616±26
SL02 <i>Porites</i> sp.	18±2	1.14±0.0015	1.4823±0.0307	999.5±20.9	146.7±1.8	0.0787±0.0003	7744±29	7711±38	150±2	7648±38
<b>Kamaran Island (old fossil corals)</b>										
KI01 <i>Porites</i> sp.	4±1	0.74 ±0.0008	4.1605±0.0836	2728.7±55.0	50.3±1.5	0.9303±0.0016	226636±1871	226485±1871	95±3	226422±1871
KI02 <i>Faviidae</i>	4±1	0.62 ±0.0009	8.123±0.1631	1054±21	-23.7±2.2	0.8437±0.0017	222169±2528	221766±2533	-44±4	221703±2533

U decay constants:  $\lambda_{238} = 1.55125 \times 10^{-10}$  (Jaffey et al., 1971) and  $\lambda_{234} = 2.82206 \times 10^{-6}$  (Cheng et al., 2013). Th decay constant:  $\lambda_{230} = 9.1705 \times 10^{-6}$  (Cheng et al., 2013).

\* $\delta^{234}U = ([^{234}U/^{238}U]_{activity} - 1) \times 1000$ . \*\*  $\delta^{234}U_{initial}$  was calculated based on <sup>230</sup>Th age (T), i.e.,  $\delta^{234}U_{initial} = \delta^{234}U_{measured} \times e^{234 \times T}$ .

Corrected <sup>230</sup>Th ages assume the initial <sup>230</sup>Th/<sup>232</sup>Th atomic ratio of  $4.4 \pm 2.2 \times 10^{-6}$ . Those are the values for a material at secular equilibrium, with the bulk earth <sup>232</sup>Th/<sup>238</sup>U value of 3.8.

The errors are arbitrarily assumed to be 50%

\*\*\*B.P. stands for "Before Present" where the "Present" is defined as the year 1950 A.D.

The tidal range in Kamaran Island is ~1 m, and datum is taken as 0.5 m.

§ living corals.

247 All samples (except Kamaran Island) are mid-Holocene in age (after correction for  
 248 detrital thorium, Table 1); samples from the top of the As-Salif salt diapir (SL01 and  
 249 SL02) are dated to  $7,616 \pm 26$  and  $7,648 \pm 38$  years BP; Ras Harafa samples (RH01  
 250 and RH02) have ages of  $5,423 \pm 47$  and  $5,324 \pm 25$  years BP; and the Om Gedi coral  
 251 sample was dated to  $4,950 \pm 30$  years BP. The two fossil corals collected from  
 252 Kamaran terraces were diagenetically altered with almost complete transformation  
 253 from pristine aragonite skeleton into calcite. These samples yielded ages of  $226,422$   
 254  $\pm 1,871$  years and  $221,703 \pm 2,533$  years BP, although the dates obtained are unlikely  
 255 to reflect the 'true' age of these samples due to the significant diagenetic alteration.

256

## 257 4.2 Reef and notch morphology

### 258 4.2.1 Al-Salif Peninsular salt diapir

259 Patch corals were found at altitude of  $+18 \pm 2$  m (apmsl) atop of As-Salif salt diapir  
 260 (Figure 2) and two coral samples (*Porites* sp.) yielded mean (inverse weighted) age of  
 261  $7,629 \pm 31$  years BP (Table 1). These samples were dated to confirm the Holocene  
 262 age of this reef and investigate local deformation due to salt diapirism. Although

263 these samples passed initial XRD screening (i.e., calcite content of < 2%), further  
264 investigation suggests U-depletion in both samples (SL01 and SL02). Further, sample  
265 SL02 has elevated  $^{232}\text{Th}$  concentration compared to modern equivalents indicative of  
266 detrital input (see section 5.1 for further discussion of the age of these samples).

267

268

269

270

271

272

273

274

275

276

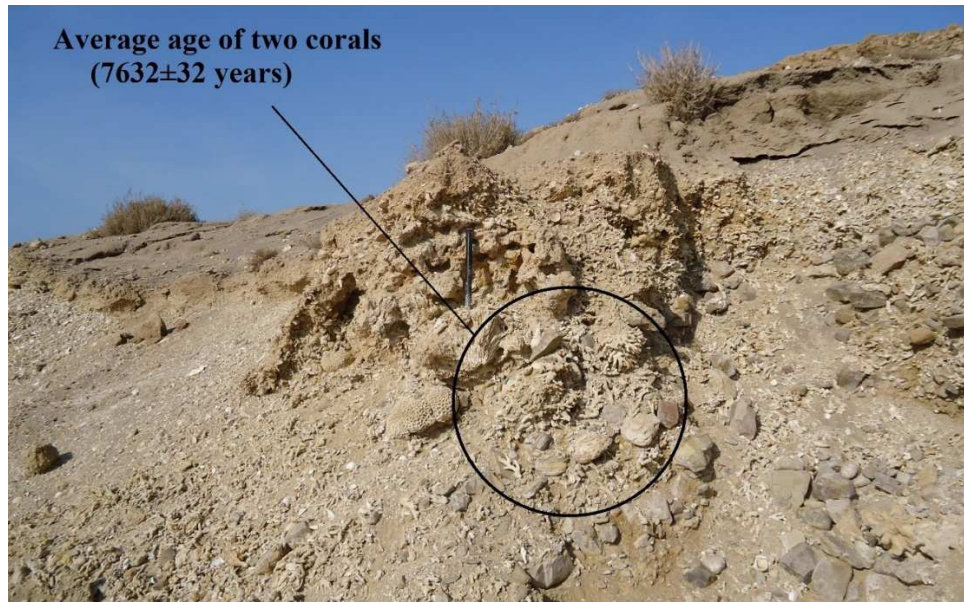


**Figure 2:** Coral samples (SL01 and SL02, circled) from the As-Salif salt diapir.

277

#### 278 4.1.2 Om Gedi terrace (OG)

279 The OG terrace has a maximum mapped elevation of  $+ 4 \pm 1$  m apmsl. It comprises  
280 an indurated aeolian (continental source) deposit, overlain by gypsiferous layer.  
281 Inspection of the OG terrace siliciclastic beach rocks indicate deposition in relatively  
282 quiet, subaerial and oxygen rich environment (fine grains and yellowish staining of  
283 the indurated sediments). The lack of reef corals at this site (i.e., the reefal limestone  
284 that overlies the Salif Formation elsewhere on the Kamaran and As-Salif Peninsula)  
285 may be due to very high terrestrial inputs and turbid-water environment that is  
286 unfavorable for large-scale carbonate production (Purser et al., 1987). A wave-cut  
287 notch mapped at  $+3 \pm 1$  m apmsl (Figure 3) and is assumed to be of Last Interglacial  
288 (Llg) age. We were unable to obtain reliable date for this feature but have assign a  
289 Last Interglacial age given the proximity and similarity in elevation to the U-series  
290 dated fossil reef at Bab al-Mandab, southern Red Sea ( $4 \pm 1$  m apmsl; Al-Mikhlaifi et  
291 al., 2018). This notch has its middle and upper portions preserved as notch roof,

292 whereas its base buried under the aeolinite sand. A Holocene cliff developed below  
 293 the Llg notch at an elevation of  $\sim +1.5$  m (Figure 3). An *in situ* *Porites* sp. coral (OG1;  
 294  $+1 \pm 0.2$  m apmsl), found intercalated with siliciclastic deposits adjacent to the  
 295 Holocene wave-cut cliff, was dated to  $4,950 \pm 30$  years BP (Table 1), and considered  
 296 equivalent in age to cliff formation (Figure 3). The shape of Holocene cliff suggests  
 297 that the cliff developed initially in the cohesionless aeolinite material and that the  
 298 roof collapsed, likely due to wave action.  
 299

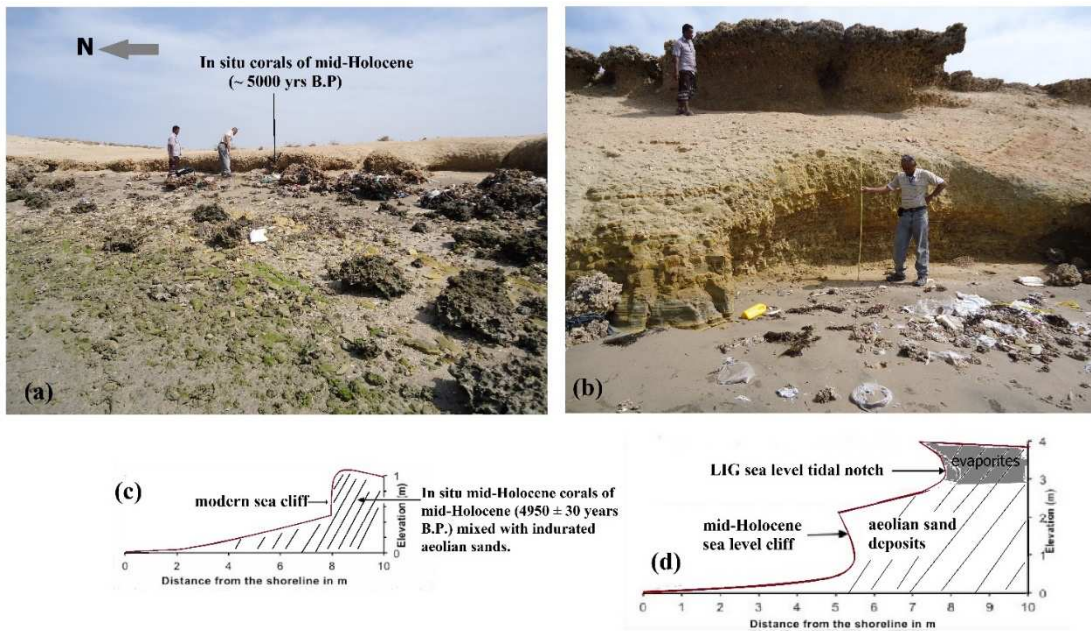


**Figure 3:** Photographs and field sketches of the Om Gedi terrace, As-Salif Peninsula. (a) An outcrop of *in situ* *Acropora* sp. of mid-Holocene age capped by siliciclastic sediments; and in the foreground, reworked boulder of gypsiferous sandstone from the main terrace (b) Photograph of mapped stratigraphic sequence showing mid-Holocene abrasion notch, with overlying Llg notch; (c) cross-section of (a) and; (d) cross-sections of (b).

300 **4.1.3 Ras Harafa (RH)**

301 RH is the northernmost terrace of As-Salif peninsula, and is the uppermost part of  
 302 the Salif Formation. It has a maximum elevation of  $+3 \pm 1$  m apmsl. The terrace is  
 303 formed of gypsum/gypsiferous clastics intercalated with fine grained siliciclastic

304 material, with gypsum deposits (likely sabkha). Again, the reef limestones that  
 305 typically overlie the Salif Formation are not represented here. Notches and  
 306 solutional caves (Figure 4b), which can indicate the position of sea level at the time  
 307 of their formation (Myroie and Carew, 1988; Florea et al., 2007), are cut into the  
 308 late-Miocene terrace (Figure 4c). Patch corals of Holocene age (RH01 and RH02; both  
 309  $+0.5 \pm 0.1$  m apmsl, Table 1) were found in a modern lagoon setting below the RH  
 310 terrace at elevation of  $\sim 0.5$  m apmsl. Recent gypsum deposits with  
 311 mushroom/stromatolites morphologies are found encrusting mid-Holocene patch  
 312 corals and are emerged during low tide (Figure 4a).  
 313

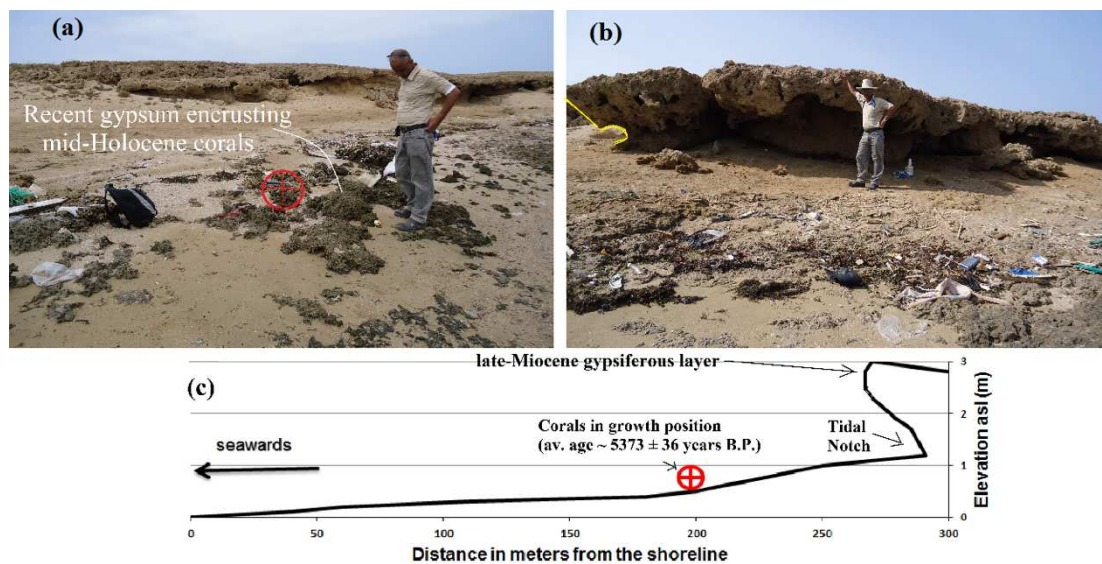


**Figure 4:** The Ras Harafa terrace, As-Salif Peninsula. (a) photograph of Holocene corals (foreground) with samples RH01 and RH02 highlighted in red. Assumed late-Miocene age terrace in the background; (b) notches/solution caves cut into late-Miocene terrace; (c) schematic cross-section of the Ras Harafa terrace.

#### 314 4.1.4 Kamaran Island (KI)

315 The Kamaran Limestone is capped with a compact and highly weathered reef  
 316 carbonate of early Pleistocene age, and contains variety of well-developed notches,  
 317 and cliff structures. The area is microtidal and has generally sheltered coastal sites  
 318 making the area promising for sea-level reconstruction.

319 In the north of the island, we documented distinct asymmetrical V-shaped notches  
 320 with inflection points of  $0.5 \pm 0.2$  m apmsl (Figure 5). The eastern part of Kamaran

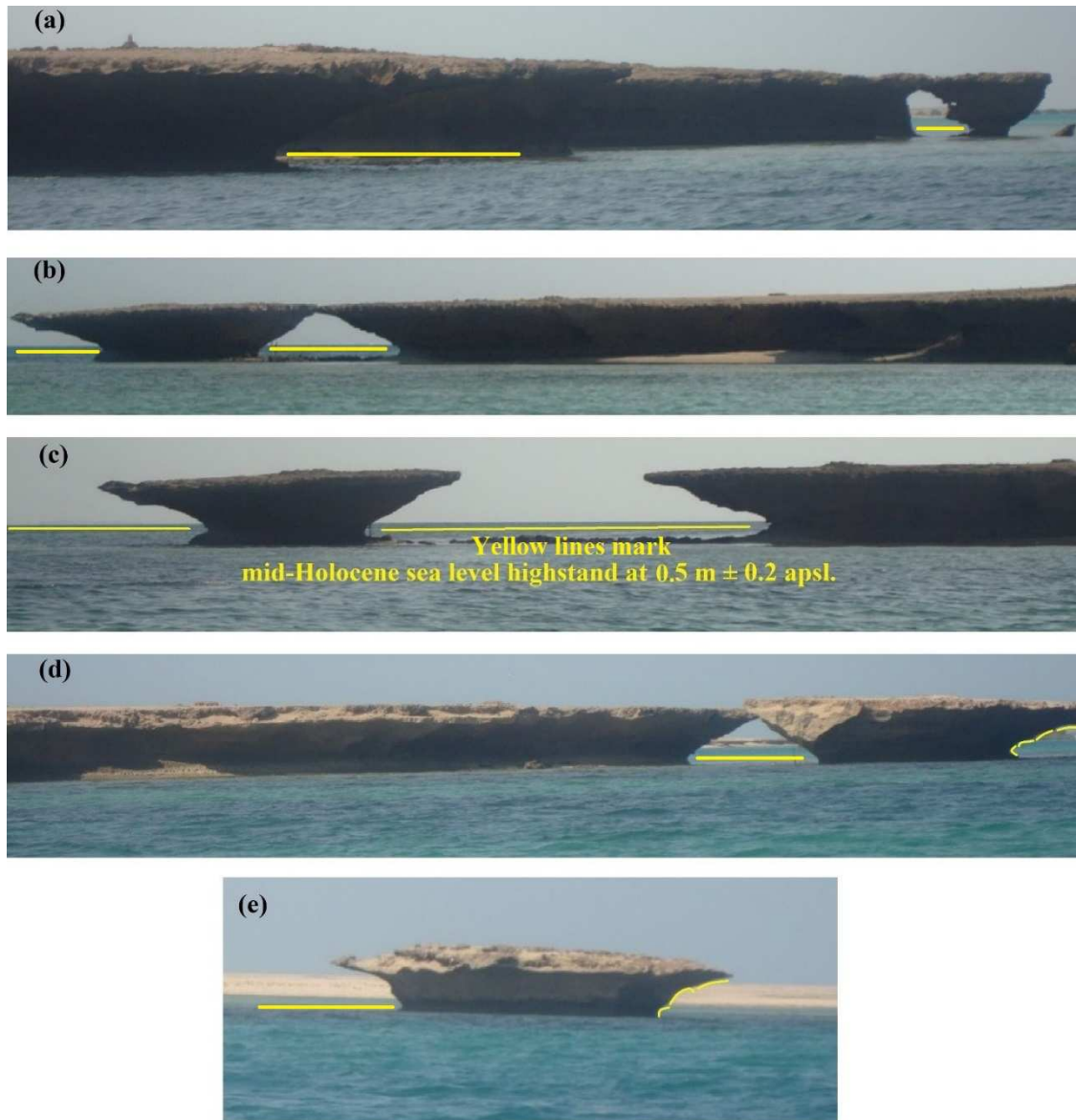
321 Island is influenced by localized (neotectonic) vertical movement of the salt diapir  
322 intrusion, with clear displacement in the elevation of surveyed geomorphic features  
323 (reverse fault evident in Figure 6a). Five sites in this location were mapped in detail.  
324 At the first site, an embryonic notch (i.e., modern) is forming at close to present sea  
325 level in the Holocene cliff (maximum elevation  $\sim 1 \pm 0.2$  m apmsl) (Figure 6b, see also  
326 map in the *Supplementary Information doi: 10.6084/m9.figshare.13079240*). At the  
327 second location (slightly to the north), a series of notches was mapped, with 4  
328 notches at elevations ranging from approximately +4 m to +2 apmsl (Figure 7a and  
329 b). This 'staircase' morphology (i.e., vertical separation of the notches) and U-shaped  
330 geometry (i.e., widening and deepening) of these notches likely resulted from  
331 vertical motion associated with coseismic uplift associated with the As Salif salt  
332 diapir (cf. [Schneiderwind et al., 2017](#)).

333 Progressing further around the bay to the north, a well-developed U-shaped notch  
334 of assumed Llg period is found at elevation of  $\sim 3 \pm 1$  m apmsl in weathered marly  
335 limestone ([Figure 8a](#)) and a V-shaped notch is well defined at  $+0.5 \pm 0.2$  m apmsl.  
336 Neither of these notches were dated but based on their elevation and comparison  
337 with other sites in the region, we assign the upper to the Llg and the lower to the  
338 mid-Holocene. *Lithophaga* boreholes in the lower unit may suggest slow uplift  
339 subsequent to the Llg period.

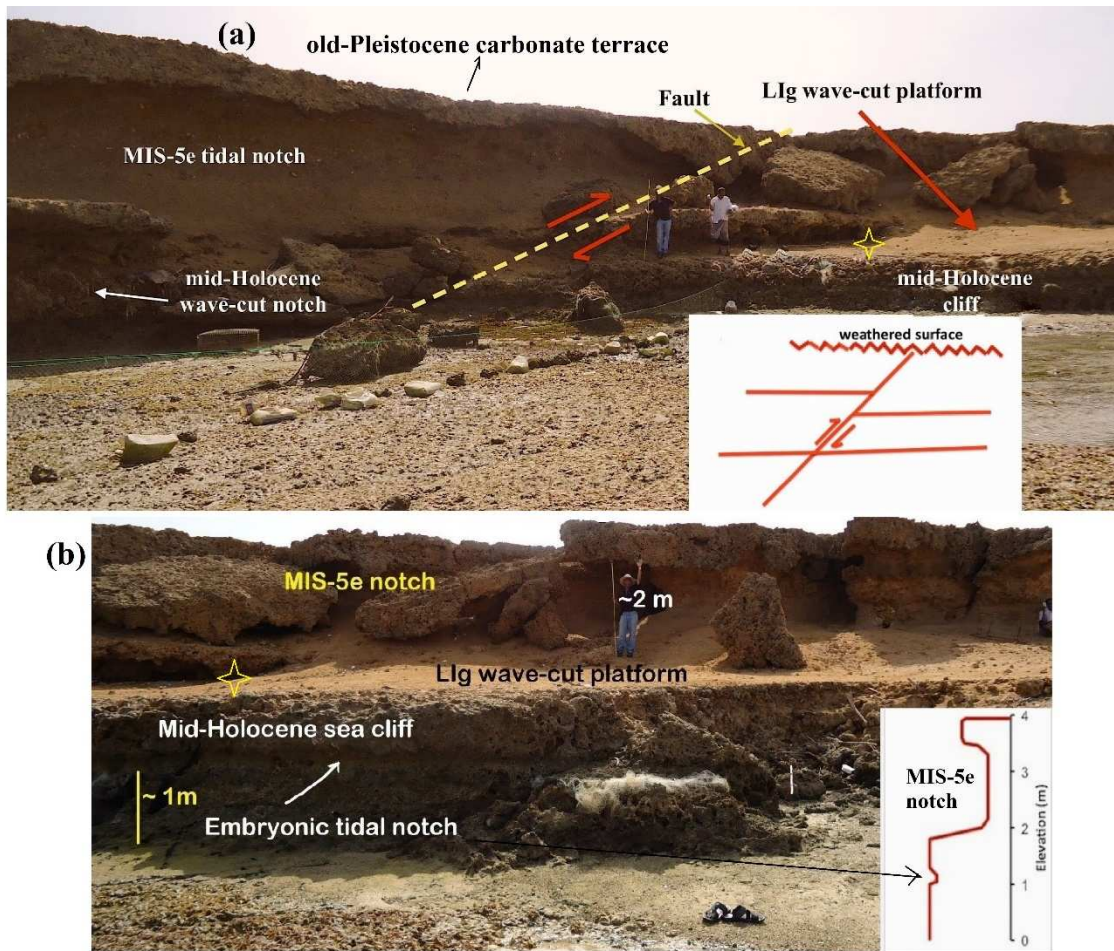
340

341 Finally, a well-developed, symmetric V-shaped wave-cut notch was observed in the  
342 uppermost section of the terrace, and corals at  $\sim +3 \pm 1$  m apmsl were selected for  
343 dating to corroborate our assumption of Llg age for notches cut at the elevation at  
344 this site ([Figure 8b](#)). Unfortunately, these corals were all highly diagenetically altered  
345 (corals KI01 and KI02, [Table 1](#)) and yielded ages of >200,000 years BP ([Table 1](#)).

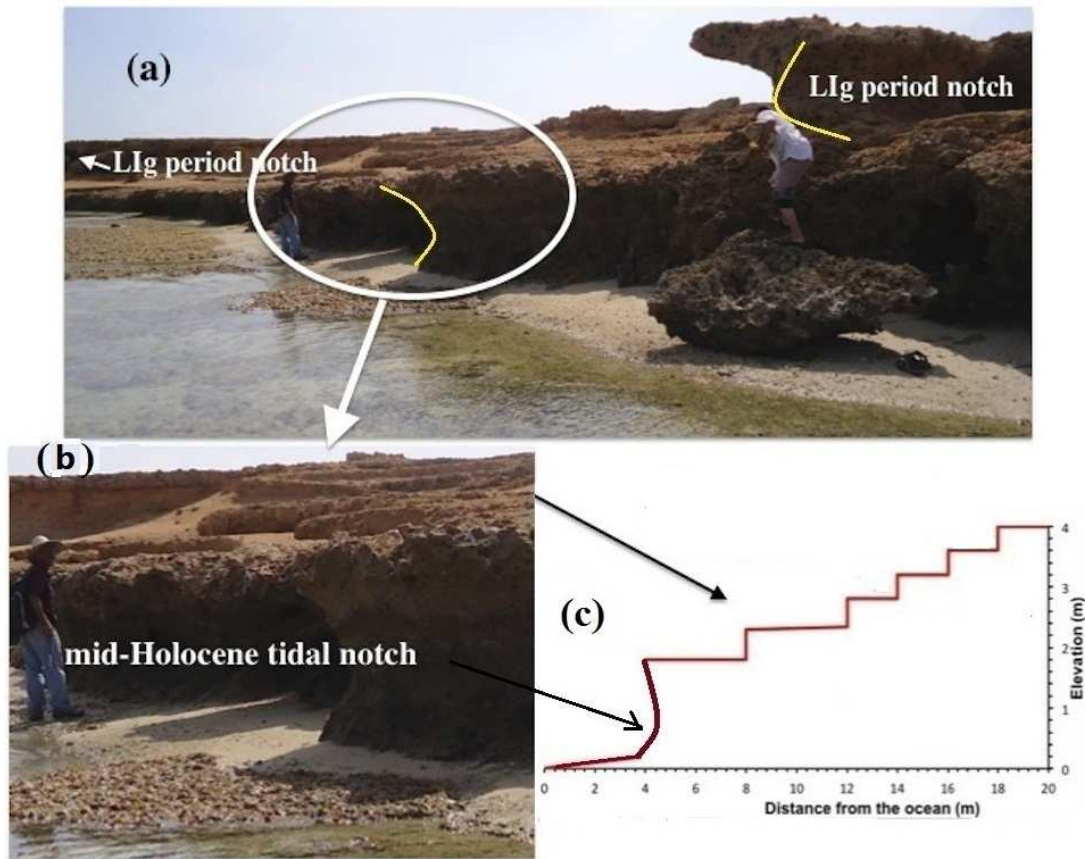
346



**Figure 5:** Wave-cut notches from the northern Kamaran Island, southern Red Sea. (a), and (b) were formed by wave action on a headland; (c), (d) and (e) sea stacks (“mushroom rocks”) with well-developed marine notches just above present sea-level, and clear indentation at  $0.5 \text{ m} \pm 0.2 \text{ apsl}$ .

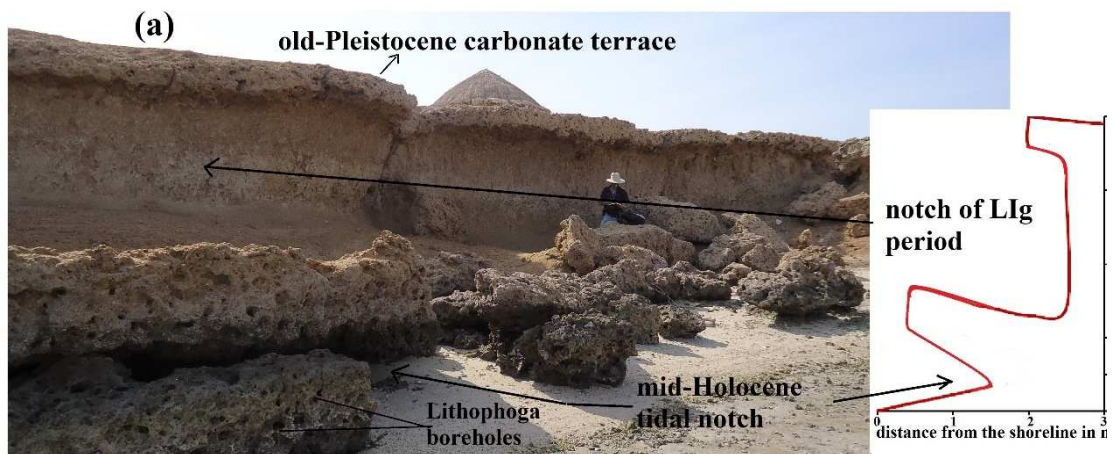


**Figure 6:** Photographs and schematic cross-sections of assumed reverse fault, eastern Kamaran Island. (a) observed reverse fault likely caused by neotectonics (schematic cross section, below right); (b) section to the right of yellow star in (a) which remained stable, showing the mid-Holocene wave-cut cliff and embryonic (modern) notch (schematic cross section, below right).



**Figure 7:** (a) Pleistocene carbonate terrace with a series of wave-cut features or sea-level oscillations ("staircase") of assumed LIg age (b) is a close up of the mid-Holocene notch; (c) schematic cross-section.

349



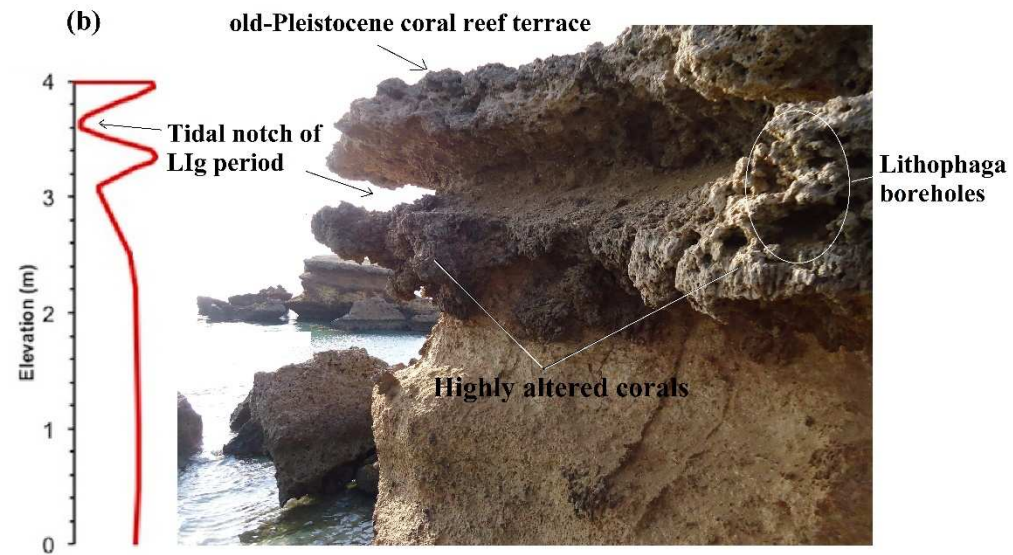


**Figure 8:** Pleistocene terrace with a U-shape of LIg wave-cut notch and V-shaped mid-Holocene wave-cut notch at  $\sim 0.5 \pm 0.2$  m below (schematic cross-section, right). (b) notch (assumed LIg age) cut into highly altered old-Pleistocene coral reefs at  $\sim 3 \pm 1$  m apmsl.

## 350 5. DISCUSSION

### 351 5.1 Reliability of U-series geochemical data

352 All samples from this study show measured  $(^{234}\text{U}/^{238}\text{U})_{\text{act}}$  close to the modern sea  
 353 water value of  $\sim 1.147$  (Stirling and Andersen, 2009), and plot on or near the  
 354 seawater evolution curve. All samples, except for those from RH, have  $^{238}\text{U}$  and  $^{232}\text{Th}$   
 355 concentrations that deviate from the live/dead corals of Bab al-Mandab (Al-Mikhlaifi  
 356 et al., 2018), modern corals from Aqaba (Scholz et al., 2004), and in the minimum  
 357 range of  $^{238}\text{U}$  concentrations of modern corals from Red Sea ( $\sim 1.3 - 4.2$  ppm)  
 358 (Hibbert et al., 2016, and references therein) (Table 1). Plotting  $^{238}\text{U}$  concentrations  
 359 versus  $(^{230}\text{Th}/^{238}\text{U})$  activity ratios (Figure 9a) provides insights into the effect of  
 360 uranium loss on the apparent ages, due to the inverse relationships between  $^{238}\text{U}$   
 361 concentrations and  $(^{230}\text{Th}/^{238}\text{U})$  activity. Similarly, plotting  $^{232}\text{Th}$  concentrations  
 362 versus  $(^{230}\text{Th}/^{238}\text{U})$  activity ratio, suggest that the effect of any uranium loss was  
 363 accompanied by thorium addition (Figure 9b). These changes probably resulted from  
 364 post depositional uranium loss, moving the data to the right on the diagram without  
 365 affecting  $(^{234}\text{U}/^{238}\text{U})$  activity (Figure 9c).

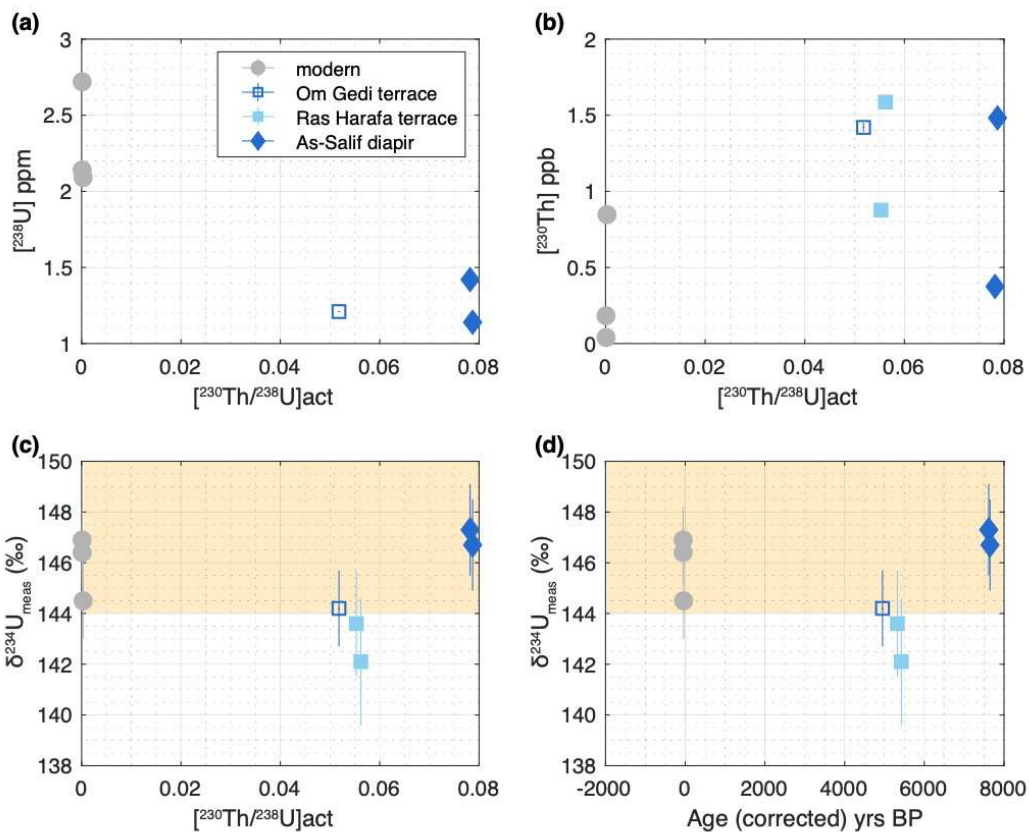


**Figure 9:** Bivariate plots of (a)  $^{238}\text{U}$  concentration vs.  $(^{230}\text{Th}/^{238}\text{U})_{\text{act}}$  of samples from As-Salif Peninsula (note, errors are smaller than the symbols); (b)  $^{230}\text{Th}$  concentration vs.  $(^{230}\text{Th}/^{238}\text{U})_{\text{act}}$  of the same samples (note, errors are smaller than the symbols); (c) Plot of  $(\delta^{234}\text{U})_{\text{meas}}$  vs.  $(^{230}\text{Th}/^{238}\text{U})_{\text{act}}$ . (d)  $(\delta^{234}\text{U})_{\text{meas}}$  vs. age of samples from the As-Salif Peninsula. The pale orange boxes represents the 'strictly reliable' values of  $(\delta^{234}\text{U})_{\text{meas}}$  for modern seawater ( $(\delta^{234}\text{U})_{\text{initial}} = 147 \pm 3$  ‰). Errors are plotted at 2 sigma.

367 The corals from the top of the As-Salif salt diapir yielded mean U-series ages of  
 368  $\sim 7,630$  years BP. These ages are in contrast to conventional radiocarbon dates of  
 369 *Tridacna* shells by Davison et al. (1996) (reported as conventional radiocarbon ages  
 370 of  $3,700 \pm 250$  and  $3,850 \pm 250$  years) from the same site and elevation. Our samples  
 371 have lower  $^{238}\text{U}$  concentrations than typical dead/live corals (2-3 ppm) and one,  
 372 SL02, also has high  $^{232}\text{Th}$  content (i.e., above the 0.5 ppb value for pristine coral  
 373 samples), which may indicate the presence of secondary contamination. Both  $^{238}\text{U}$

374 loss and  $^{232}\text{Th}$  high would increase the age and account for the offset with the  
375 radiocarbon ages of the *Tridacna* shells.

376

## 377 **5.2 Notches as sea-level indicators in the southern Red Sea**

378 Abrasion by wave and currents can create permanent wave-cut notches that, if  
379 preserved, can be useful palaeo sea-level indicators. Notches manifest as  
380 indentations or undercuts of a few centimetres to several meters (Antonioli et al.,  
381 2017) and form at or near mean sea level, during (a) prolonged stand-stills, and/or  
382 (b) when the rates of erosional processes are in line with the pace of relative sea-  
383 level change (Antonioli et al., 2006; Evelpidou et al., 2012). They are formed via  
384 chemical dissolution processes, wetting and drying cycles, biological erosion, wave  
385 action, or more likely, a combination of these factors (Antonioli et al., 2015). Often  
386 their vertical extension almost equals the tidal range (e.g. Pirazzoli, 1986). As a  
387 result, notches can serve as accurate sea-level indicators, especially in tectonically-  
388 stable regions (Neumann and Hearty, 1996; Antonioli et al., 2006; Hearty et al.,  
389 2007; Rodríguez-Vidal et al., 2007). However, in tectonically stable settings, wave-cut  
390 notches that were created in the late Pleistocene can be reoccupied and modified in  
391 the late-Holocene by sea level and associated wave action that reach similar  
392 elevations (Phillips, 1970; Trenhaile, 1972; Kelsey, 1990; Kelsey and Bockheim,  
393 1994). Notches can also form from other (often interrelated) processes including  
394 eustatic/isostatic sea-level adjustments, tectonic and seismic processes (Carobene,  
395 2015), as well as the action of chemical, physical, and biological factors (Pirazzoli,  
396 1986, Antonioli et al., 2015).

397

398 A major limitation of using wave-cut notches as sea-level indicators is the difficulty in  
399 directly dating their formation. The dating of organisms that form the biological rim  
400 covering part of the notch (Pirazzoli et al., 1994a; Pirazzoli et al., 1994b; Faivre et al.,  
401 2013) or correlating the elevation of a notch with other datable markers has proved  
402 fruitful. An alternative approach, which we adopt here, assumes dates from corals  
403 found on the platform immediately below the notch are coeval with notch formation  
404 (Lorscheid et al., 2017). Unfortunately, we were unable to obtain ages for the older  
405 notches (elevation ~3 to + 4 m apmsl) as the corals showed significant diagenetic

406 alteration and were unsuitable for dating. We therefore assume all notches at  
407 approximately +4 m apmsl that directly overlie the mid-Holocene notches, date to  
408 the Llg.

409

410 For the sites investigated, we found that some terraces are better preserved and less  
411 eroded than others, and this is mainly dependent on the rock lithology and hydraulic  
412 regime at each site. Sheltered beaches are more likely to develop notches than  
413 beaches with aggressive hydraulic regime. We attribute the differences in  
414 preservation/morphology of the features mainly to variation in tectonic activity of  
415 the region, resistance of the rock, the time the rocks were exposed to wave attack,  
416 and the variable occurrence of structural discontinuities such as cracks, fissures,  
417 joints, bedding planes, and faults (cf. [Lorscheid et al., 2017](#)). Variations in  
418 morphology (height, depth and shape) of the modern and fossil notches may also  
419 arise if the rate of erosion is not gradual and continuous (cf. [Pirazzoli and Evelpidou,](#)  
420 [2013](#)), or from exposure to sub-aerial weathering by coseismic activity ([Stiros et al.,](#)  
421 [2009](#), [Pedoja et al., 2014](#)).

422

423 At the tectonically stable Ras Harafa (RH) site, the sea cliff has a pronounced  
424 cave/large notch at  $+ 2 \pm 1$  m apmsl (inferred Llg age) which may have been  
425 reoccupied during the late Holocene (Figure 10). This may suggest negligible GIA-  
426 induced net relative sea-level change from one highstand to the next (Llg and  
427 Holocene) and/or limited influence of tectonics, including salt diapirism in the area.

428



**Figure 10:** Photograph of the Ras Harafa terrace with Llg notch/cave at  $\sim+2 \pm 1$  m apmsl; the yellow line is the highest tidal range.

429 In contrast, the preserved notch and sea cliff cut into the OG terrace, which is  
430 located closer to the As-Salif salt diapir, are distinctly separated in elevation (notches  
431 at  $\sim+3 \pm 1$  m of inferred Llg age, and a mid-Holocene sea cliff at  $+1\pm 0.2$  m) (Figure  
432 3b), with differences in host rock lithology having a strong control on their  
433 morphology. The Llg notch is carved into evaporite rocks, whereas the modern sea  
434 cliff is cut into poorly cemented recent aeolinite sand deposits. The Llg notch has  
435 additional structure, with middle and upper notch roofs preserved. The notch floor,  
436 however, is buried under aeolinite sand deposit making it difficult to measure the  
437 notch height, but this is clearly greater than the maximum modern tidal range. This  
438 could be a consequence of greater tidal range during the Llg, or a sequence of  
439 stillstands. The late Holocene sea cliff developed at the toe of Llg notch and probably  
440 formed as the result of abrasion processes where sediment entrained in waves or in  
441 turbulent broken wave bore, rushes up the beach face, excavating a “basal notch”  
442 and leaving the overhanging cliff material undermined, leading to failure (Bird,  
443 2000). This process is promoted by the presence of groundwater in the cliff material  
444 (May and Heeps, 1985) and bioerosion (Trenhaile, 1987).

445

446 On Kamaran Island, a series of geomorphic structures - fossil coral terraces, wave cut  
447 platform, notches, and sea cliffs (Figure 6) – record past sea-level changes. A  
448 Holocene sea cliff is cut into indurated Pleistocene carbonate rocks at elevation of 1  
449  $\pm 0.2$  m apmsl. This has a composite structure with an embryonic notch forming at  
450 modern sea level (Figure 6b). The embryonic notch was found at elevations of  
451 approximately the highest modern tidal range ( $\sim 1$  m) and have ‘overprinted’ the  
452 mid-Holocene sea cliff (Figure 6b). This may indicate that the proto-notch starts at  
453 the highest tidal range and is developing up/down with slow terrace uplift. The  
454 geomorphological characteristics of these notches, i.e., cut at modern high-tide into  
455 the vertical Holocene cliff of carbonate bedrock with a symmetric flattened U-shape,  
456 may be the result of quiescent conditions during the early stages of notch  
457 development. Such overlapping of the former and new erosional zones in Kamaran

458 Island (Figure 6b) corroborates the site's tectonic stability as the former erosional  
459 surface does not exceed the modern tidal range. It also suggests that the Kamaran  
460 Island has been stable for a considerable time (i.e., for at least the late Pleistocene).  
461 Another notch at  $\sim +4 \pm 1$  m apmsl (Figure 8b) is thought to be of Llg age, although  
462 corals sampled from this terrace were diagenetically altered and yield older ages  
463 than the Llg (Table 1).

464

465 A quantitative relationship between notch size, wave energy, and lithology has been  
466 suggested (e.g., [Antonioli et al., 2015](#)). These authors show that the vertical distance  
467 between the roof and the base of the notch is greater than the mean tidal range, but  
468 smaller than the maximum difference between tidal extremes (i.e., the maximum  
469 and minimum tides). However, this relationship may not be maintained for all  
470 notches, and it is not uncommon for notches to have height greater than the tidal  
471 range, and up to 3.2 times the tidal range in sheltered/exposed sites ([Antonioli et al.,](#)  
472 [2015](#)). Nonetheless, several studies have linked the width of wave-cut notches (i.e.,  
473 the vertical distance between the base and the roof) to the amplitude of the mean  
474 tidal range ([Trenhaile et al., 1998](#); [Antonioli et al., 2015](#); [Trenhaile, 2015](#); [Rovere et](#)  
475 [al., 2016](#); [Lorscheid et al., 2017](#)). For example, where the height of the notch is  
476 greater than the modern tidal range and assuming the notch was formed by similar  
477 processes to today, the difference in the modern and palaeo notch amplitudes can  
478 be related to changes in tidal range (e.g., [Antonioli et al., 2015](#); [Lorscheid et al.,](#)  
479 [2017](#)). Such comparisons provide a first-order estimate of possible changes in tidal  
480 amplitudes.

481

482 The notches in eastern Kamaran have U-shape morphologies (i.e., notch height  
483 exceeds the notch depth), which is greater than the modern tidal range of the area  
484 ( $\sim 1$  m). When coupled with the U-notch morphology with the staircase morphology  
485 from the same sites (Figure 7), this suggest co-seismic activity, as these terraces lie  
486 within the As-Salif Diapir zone. However, sea-level oscillations and/or a sequence of  
487 sea-level stillstands related to-differences in the tidal regime cannot be excluded.  
488 Alternatively, the U-shaped morphologies could suggest that the Llg notches (+3 to  
489 +4 m apmsl) were deeper originally, but weak host rocks and prolonged weathering

490 led to shape modification and roof collapse. The presence of failed cliff material  
491 deposited at the toe of Kamaran Island sea cliffs (Figures 6 to 8) would support this  
492 interpretation. Deeper notches would require a prolonged contact and/or weak host  
493 rocks. Coseismic activity related to the As-Salif salt diapirism to the east of Kamaran  
494 Island could also have led to notch displacements and collapse.

495

### 496 **5.3 Mid-Holocene sea-level highstand(s)**

497 The global record of mid-Holocene sea level is complex and geographically divergent  
498 due to glacio-hydro-isostatic and water redistribution processes (e.g., ocean  
499 syphoning at the end of the dominant melting period ~6 to 7 ka) (Clark et al., 1978;  
500 Pirazzoli and Pluet, 1991; Mitrovica and Peltier 1991; Mitrovica and Milne, 2002;  
501 Lambeck et al., 2014). A sharp decrease in the rate of sea-level rise is predicted after  
502 ~6.8 ka, with low rates of change ( $> 1.42$  mm/yr) for the remainder of the Holocene  
503 (Antonioli et al., 2015 and references therein). The combined deformation and  
504 gravitational response resulted in divergence in the timing and amplitude of the mid-  
505 Holocene highstand globally (Nakada and Lambeck, 1987; Pirazzoli and Pluet, 1991;  
506 Long, 2001; Mitrovica and Milne, 2002; Milne et al., 2009; Stategger et al., 2013;  
507 Woodroffe and Webster, 2014; Lambeck et al., 2014). A spatially complex pattern is  
508 also predicted from the Red Sea, where the isostatic response is largely determined  
509 by water-loading (Red Sea, Indian Ocean and Mediterranean) (Lambeck et al., 2011).

510

511 Mid-Holocene highstands have been reported for several locations within the Red  
512 Sea. The complex spatial variability is expected due to the hydro-isostatic response  
513 in the basin to time-dependent water loading (Lambeck et al., 2011). GIA predictions  
514 for the Red Sea (e.g. Lambeck et al., 2011; Lambeck et al., 2012) produce high sea  
515 levels when ice melt was at its maximum rate, and the highstand is predicted to be  
516 more pronounced for both ends of the Red Sea regions compared to the central  
517 basin due to water loading from the Indian Ocean and the Mediterranean (Lambeck  
518 et al., 2011). In addition, as the glacio-isostatic signal is of the opposite sign to sea-  
519 level rise due to melt, mid-Holocene sea-level highstands are not expected for all  
520 locations in the Red Sea (Lambeck et al., 2011). Our well-constrained sea-level

521 indicators, and a compilation of previously reported mid-Holocene highstand data  
522 (Friedman, 1968, Faure, 1975; Hötzl et al., 1984; Dabbagh et al., 1984; Al-Rifaiy and  
523 Cherif, 1988; Gvirtzman et al., 1992; Gvirtzman, 1994; Dullo and Montaggioni, 1998;  
524 Plaziat et al., 1995, 1998; El-Asmar, 1997; Carbonne et al., 1998; Moustafa et al.,  
525 2000; Shaked et al., 2004) (Figure 11), provide a valuable test of GIA models, Earth  
526 model parameter choices for this region, and sea-level predictions given that sea-  
527 level amplitudes are strongly Earth model dependent (~1 m at our study sites), with  
528 strongest dependence on the upper mantle viscosity (Lambeck et al., 2011). The data  
529 from the Yemeni Red Sea are especially useful as to date, observational data is  
530 scarce for the southern Red Sea.

531

532 U-series ages of coral samples from two locations on the As-Salif Peninsula (RH and  
533 OG) indicate that the terraces and associated geomorphological features are mid-  
534 Holocene in age, whereas the corals dated from the ~4 m terrace on Kamaran Island  
535 where highly altered and are assumed to be of Last Interglacial in age (Table 1). Our  
536 sites on the As-Salif Peninsula suggest some diapir influence, but that this diminishes  
537 away from the locus of the diapir, with successively less influence on the elevations  
538 of the Om Gedi and Ras Harafa terraces respectively. The two in growth position  
539 corals ( $+0.5 \pm 0.2$  m apmsl) from the Ras Harafa terrace have mid-Holocene ages  
540 ( $5,358 \pm 33$  years BP, inverse weighted mean), and are likely a maximum estimate of  
541 the age of the mid-Holocene highstand in this region of the southern Red Sea, given  
542 that they are below the maximum elevation of the notch cut into the same terrace.  
543 The notch itself likely represents the upper limit (elevation  $+1 \pm 0.2$  m apmsl, Figure  
544 4) of the mid-Holocene sea-level highstand (i.e., mean sea level) at this site.

545

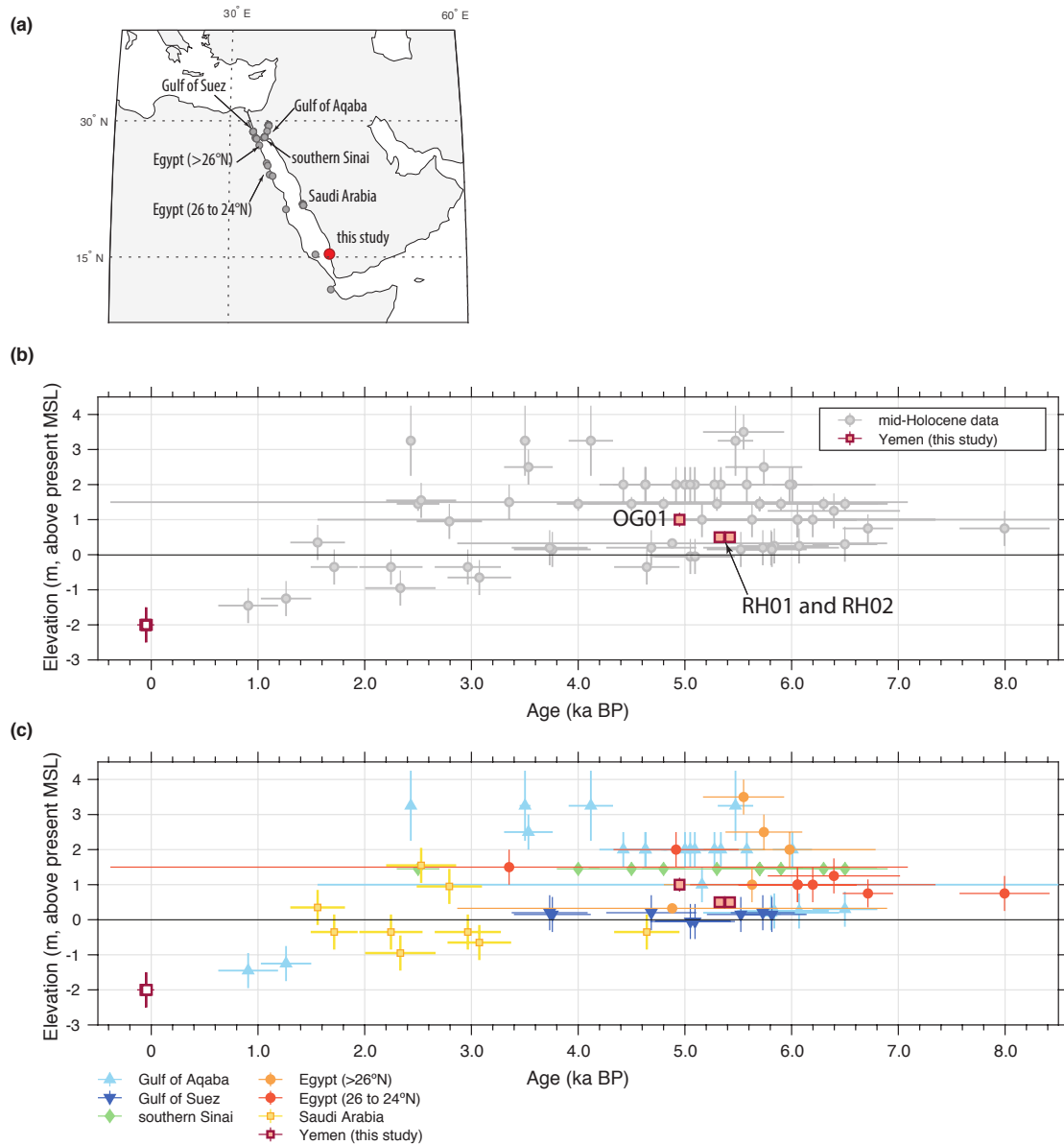
546 Our new data are broadly consistent with other mid-Holocene sea-level data for the  
547 Red Sea (Figure 11), and show the drop in relative sea level after the cessation of the  
548 main melt period at ~6 ka (Nakada and Lambeck, 1987; Mitrovica and Milne, 2002;  
549 Antonioli et al., 2015; Lambeck et al., 2014). In general, the more northerly sites  
550 have higher elevation mid-Holocene terraces, and older ages for the terraces than  
551 for the sites in Saudi Arabia at the centre of the basin (Figures 11 and 12) (Friedman,

552 [1968](#); [Gvirtzman, et al., 1992](#); [Gvirtzman, et al., 1994](#); [El-Asmer, 1997](#); [Dullo and](#)  
553 [Montaggioni, 1998](#); [Plaziat et al., 1998](#); [Moustafa et al., 2000](#); [Shaked et al., 2002](#);  
554 [Faur, 1975](#); [Hötzl et al., 1984](#); [Hein et al., 2011](#)), which is in broad agreement with  
555 GIA predictions for the mid-Holocene ([Lambeck et al., 2011](#)). Our new Yemen data  
556 also show older ages for the southern edges of the basin, and the elevation of the  
557 highstand is close to that predicted ( $\sim 0.5$  m) using the preferred Earth model (E3) of  
558 [Lambeck et al. \(2011\)](#). In detail, the elevation of our Yemen samples is very similar  
559 to the elevations given for the fossil terraces of Saudi Arabia ([Dullo and Montaggioni,](#)  
560 [1998](#)), where a “lower” highstand is predicted, and also similar in elevation to  
561 portions of the Egyptian coast (24 to 26 °N; [Plaziat et al., 1995, 1998](#)), where a  
562 “higher” highstand are predicted from GIA modelling (cf. [Lambeck et al., 2011](#)).  
563 There may be tectonic, or neotectonic (e.g., due to salt diapirism) overprinting of the  
564 elevations and sea-level signal at other sites, but which have been explicitly  
565 accounted for in our study using local and regional mapping. This allowed us to  
566 disentangle the neotectonic overprinting and to determine the most likely elevation  
567 for the mid-Holocene highstand at the Ras Harafa site (i.e., the elevation of the  
568 notch at elevation  $+1 \pm 0.2$  m apmsl, [Figure 4](#)). Further data from the Red Sea, and  
569 the southern Red Sea in particular, is needed to more fully test the GIA models and  
570 associated sea-level predictions. A sufficiently dense geographical coverage is still  
571 lacking, and factors other than sea level (e.g., neotectonics) need to be disentangled  
572 by careful mapping at local/regional scales.

573

574 In summary, our observations from the southern Red Sea, compare favorably with  
575 the GIA prediction models of [Lambeck et al. \(2011\)](#), where the highest and earliest  
576 mid-Holocene sea levels occur between 6 to 5 ka in the southern (and northern) Red  
577 Sea basin and also with other observational data ([Friedman, 1968](#), [Faur, 1975](#); [Hötzl](#)  
578 [et al., 1984](#); [Gvirtzman et al., 1992](#); [Gvirtzman, 1994](#); [Dullo and Montaggioni, 1998](#);  
579 [Moustafa et al., 2000](#); [Shaked et al., 2002](#); [Hein et al., 2011](#)) from the basin (Figure  
580 12). However, more high-quality data, with well constrained age and elevation  
581 uncertainties, is required to more fully test both the GIA predictions and Earth model  
582 parameter choices for the region.

583



584

585 **Figure 11:** Elevation of the mid-Holocene highstand in the Red Sea. (a) map of mid-  
 586 Holocene highstand sites (b) grey dots, reported mid-Holocene elevations and ages  
 587 (Friedman, 1968, Faur, 1975, Hötzl et al., 1984; Gvirtzman, 1994; Gvirtzman et al.,  
 588 1992; Dullo and Montaggioni, 1995, 1998; Al-Raifaiy and Cherif, 1988; Moustafa et al.,  
 589 2000; Shaked et al., 2002; Hein et al., 2011) (radiocarbon ages have been  
 590 recalibrated using the latest calibration curve (Marine20, Heaton et al., 2020) and a  
 591 consistent  $\Delta R$  (weighted mean  $\Delta R = 176 \pm 62$  years ( $n = 9$ ), Cember, 1989; Felis et al.,  
 592 2004; Reimer and Reimer, 2020); filled red squares, dated fossil from As-Salif  
 593 Peninsula and, open red squares, dated modern coral samples from Bab El-Mandab;  
 594 (c) as in (b) but separated geographically by latitude. Uncertainties in age and

595 elevation are 2 sigma. (The compiled data is available here: doi:  
 596 10.6084/m9.figshare.13079240)  
 597

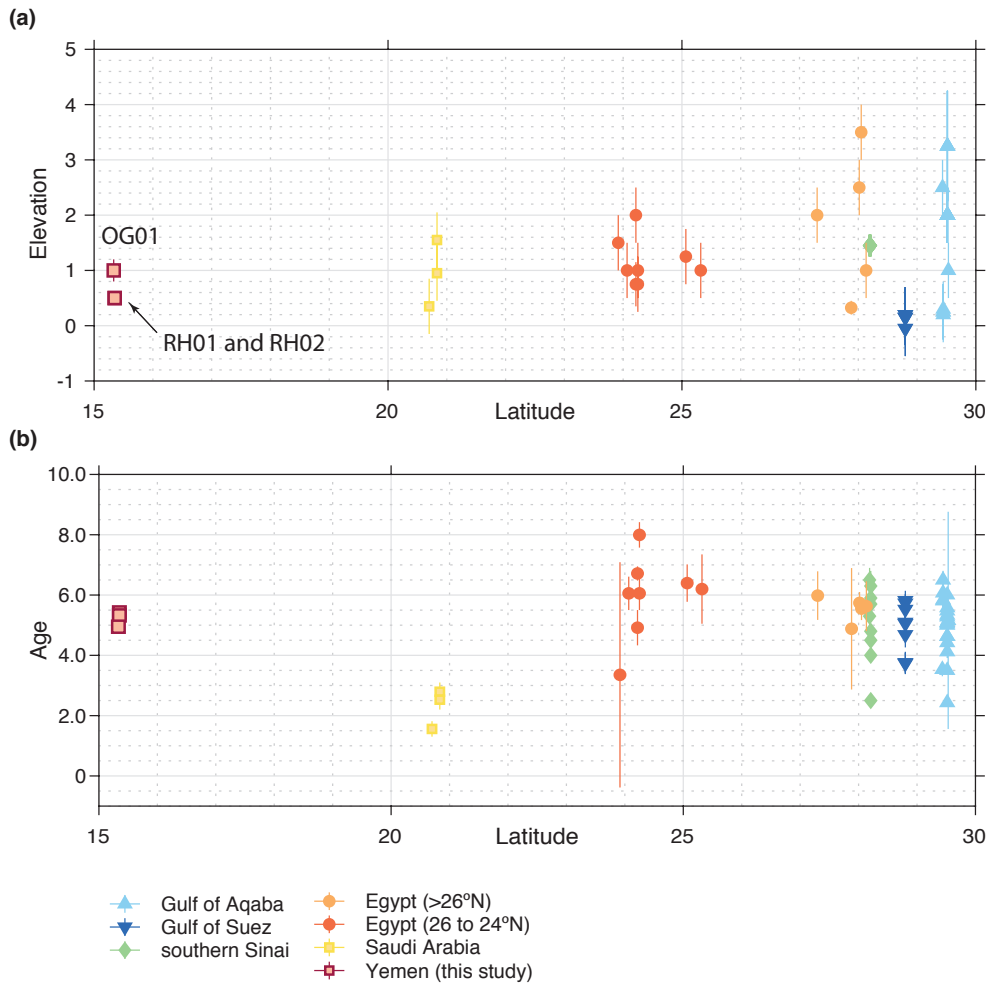


**Figure 12:** Elevation of the mid-Holocene highstand in the Red Sea. (a) grey dots, reported mid-Holocene elevations and ages (Friedman, 1968; Faur, 1975; Hötzl et al., 1984; Gvirtzman et al., 1992; Gvirtzman, 1994; Dullo and Montaggioni, 1995, 1998; El-Asmar, 1997; Moustafa et al., 2000; Shaked et al., 2002; Hein et al., 2011) (radiocarbon ages have been recalibrated using the latest calibration curve (Marine20, Heaton et al., 2020) and a consistent  $\Delta R$  (weighted mean  $\Delta R = 176 \pm 62$  years ( $n = 9$ ), Cember, 1989; Felis et al., 2004; Reimer and Reimer, 2020); red squares, elevations of dated coral samples, this study; (b) as in (a) but separated geographically by latitude. Uncertainties in age and elevation are 2 sigma. (The compiled data is available here: doi: 10.6084/m9.figshare.13079240).

#### 598 **5.4 Tectonic Stability, neotectonics and salt diapirism in the Yemeni Red Sea**

599 The development of the southern Red Sea islands and volcanic coastal formations  
600 has been primarily controlled by tectonics since the opening of the rift (Purser and  
601 Hötzl, 1988; Bosworth, 1994, 2015; Bosence, 2005; Rowlands and Purkis, 2015). Our  
602 study area (Kamaran and As-Salif Peninsula) is part of a salt diapir platform formed  
603 by a linear north-south trending salt diapir, which is bounded by a normal growth  
604 fault on the eastern margin and continues offshore for several kilometers (Bosence  
605 et al., 1998). The orientation of the island terraces in the southern Red Sea are  
606 closely related to fault lineaments, and the fault trends are also allied with swarm of  
607 high magnitudes earthquakes along the offshore of Kamaran and As-Salif regions.

608

609 The Yemeni Red Sea generally has lower seismicity and uplift compared to the  
610 northern part of the Red Sea and tectonic movements here are more localized and  
611 associated with salt diapirism. Seismic activity and tensional movements in the  
612 study region have stimulated the evaporites to rise and form a salt dome  $\sim +18$  m  
613 apmsl. The underlying evaporite unit makes the sites are more susceptible to  
614 localized crustal movements due to salt tectonics (Bosence et al., 1998). However,  
615 the influence of salt diapirism and/or tectonics appears limited and highly localized  
616 in the area, given the similarity in the elevation of the mid-Holocene notches on the  
617 As-Salif Peninsula (RH and OG), and Kamaran Island ( $+0.5 \pm 0.2$  m apmsl). However,  
618 we detect some limited neotectonism at the eastern Kamaran Island site, where the  
619 terrace is uplifted up to  $\sim +6 \pm 1$  m (apmsl) relative to the main island, which has an  
620 elevation of  $\sim +4 \pm 1$  m (apmsl) (Figure 6a). The contrast in the faults flank elevations  
621 was a result of movement of the hanging-wall (seaward side) up relative to the  
622 stable footwall (landward side), suggests a thrust (reversed) fault. The fault can be  
623 easily traced as a discrepancy between the mid-Holocene wave cut cliff (at  $\sim +1.3 \pm$   
624  $0.2$  m elevation) and the well-developed U-shape mid-Holocene wave-cut notch of  $\sim$   
625  $+2.3 \pm 0.2$  m elevation. As the displaced layer is imprinted with an embryonic notch  
626 at the same height as the sea, the age of this fault is not older than the mid-  
627 Holocene, and is probably linked with the complex activity of the salt diaper.

628

629 Northern Kamran Island is sufficiently far from the influence of the salt diapir that

630 the notches retain their asymmetrical V-shape. This is in contrast to the eastern  
631 portion of the island where coseismic activity associated with salt diapirism has likely  
632 contributed to modified the morphology of wave-cut cliffs and notches resulting in  
633 U-shaped notches. The change in the erosional base (which is limited by the tidal  
634 range) may also have been prompted by changes in sea level, wave energy and/or  
635 tidal regime leading to a widening, deepening and separation of notches and  
636 possible overprinting of older features (Schneiderwind et al., 2017).

637

## 638 **6. CONCLUSIONS**

639 We document palaeo sea-level indicators (fossil terraces, wave-cut notches and sea  
640 cliffs) for two locations (As-Salif and Karaman Island) in the Yemeni southern Red Sea  
641 and, using U-series dates of fossil corals in the same (underlying) unit, quantify the  
642 changes in sea level during the mid-Holocene and Llg. The spatial distribution,  
643 morphology and elevations of fossil terraces allowed us to disentangle the various  
644 processes, including the history of recent tectonic uplift. The relative consistency of  
645 the mid-Holocene geomorphic features suggests relative tectonic stability of the  
646 region with some minor diapir influence. These new observations improve our  
647 understanding of the local and regional history, providing constraints on the long-  
648 term rates of vertical movement that underpin models of Red Sea rifting.  
649 Additionally, given the relatively stable tectonic setting for the last ~6,000 years, the  
650 study locations, should be useful for reconstructing past sea-level changes.

651

652 We demonstrate the potential of tidal notches for reconstructing past changes in sea  
653 level in the region. Despite complications in the field (i.e., the obstruction of the  
654 vertex due to cliff failure), our new observations and detailed mapping of  
655 geomorphic features enabled us to account for neotectonics (e.g., salt diapirism,  
656 localised faulting). This allowed us to establish the elevation of the mid-Holocene  
657 highstand from wave-cut notches at  $\sim 1 \pm 0.2$  m (apmsl).

658

659 Our new southern Red Sea data thereby provide a valuable calibration dataset for  
660 geophysical models of the region, particularly as data for the southern Red Sea basin  
661 was previously lacking. Our new data, and compilation of the wider regional mid-

662 Holocene data suggest that the preferred Earth model parameters of [Lambeck et al.](#)  
663 [\(2011\)](#) provide sea-level predictions that are consistent with the available evidence.  
664 Our data go some way to addressing the ‘incomplete record’ of Holocene sea-level  
665 change in the Red Sea identified by [Lambeck et al. \(2011\)](#). However, more high-  
666 quality data is required.

667

668 The Yemeni Red Sea generally has lower seismicity and uplift compared to the  
669 northern part of the Red Sea, and tectonic movements here are more localized and  
670 associated with salt diapirism. However, some limited neotectonism in the eastern  
671 portion of the island has likely contributed to modify the morphology of wave-cut  
672 cliffs and notches resulting in U-shaped notches.

673

674

#### 675 **Acknowledgements**

676 This project was funded by U.S Fulbright program and is a research scholarship given  
677 to the first author. The help extended by Prof. Mohammed Al-Wosabi and Dr. Aref  
678 Al-Sageer during the fieldwork is gratefully acknowledged. Many thanks go to Julie  
679 Retrum, Mellissa Cross, Yanbin for their help during U-isotope analysis at the  
680 University of Minnesota. Special thanks go to Rick Knurr for assistance in XRD  
681 analysis. Einas Al-Alimey, a Cultural Affairs Specialist at the U.S Embassy in Sana’a  
682 was of great help to this study. We are most grateful to Christopher Hein (Virginia  
683 Institute of Marine Science) for detailed reviews and comments that led to  
684 substantial improvements to this work.

685

#### 686 **References**

- 687 Al-Mikhlaifi, A.S., Edwards, R.L., Cheng, H., 2018. Sea-level history and tectonic uplift  
688 during the last-interglacial period (LIG) inferred from the Bab al-Mandab coral  
689 reef terraces, Yemen, *J. Afr. Earth Sci.*, 138, 133-148.
- 690 Al-Nakhal, H. and Alaug, A.S., 2013. Nomenclature review of the rock units in the  
691 stratigraphic lexicon of Yemen, *Iranian Journal of Earth Sciences*, 5: 82-99.
- 692 Al-Rifaiy, I., Cherif, O., 1988. The fossil coral reefs of A1 Aqaba, Jordan. *Facies* 18: 219  
693 - 230. doi:10.1007/BF02536801.

694 Andersen, M.B., Stirling, C.H., Potter, E.K., Halliday, A.N., Blake, S.G., McCulloch,  
695 M.T., Ayling, B.F., O'Leary, M.J., 2010. The timing of sea-level high-stands during  
696 Marine Isotope Stages 7.5 and 9: constraints from the uranium-series dating of  
697 fossil corals from Henderson Island. *Geochim. Cosmochim. Acta* 74, 3598–3620.

698 Angelucci, A., Boni, C.F., Bono, P. et al., 1985. L'archipelago delle Isole Dahlak nel Mar  
699 Rosso meridionale: alcune caratteristiche geologiche. *Bollettino della Societa*  
700 *Geografica Italiana*, Ser. XI, Vol. II, 233- 262.

701 Angelucci, A., Matteucci, R., Praturlon, A., 1981. Outline of geology and sedimentary  
702 environments of the Dahlak Islands (southern Red Sea): *Bollettino della Societa*  
703 *Geografica Italiana*, v. 99, pp. 405-419, Roma.

704 Antonioli, F., Anzidei, M., Amorosi, A., Lo Presti, V., Mastronuzzi, G., Deiana, G., De  
705 Falco, G., Fontana, A., Fontolan, G., Lisco, S., Marsico, A., Moretti, M., Orrù,  
706 P.E., Sannino, G.M., Serpelloni, E., Vecchio, A., 2017. Sea-level rise and  
707 potential drowning of the Italian coastal plains: flooding risk scenarios for  
708 2100. *Quat. Sci. Rev.* 158, 29-43.  
709 <https://doi.org/10.1016/j.quascirev.2016.12.021>.

710 Antonioli, F., Ferranti, L., Lambeck, K., Kershaw, S., Verrubbi, V., Dai Pra, G., 2006.  
711 Late Pleistocene to Holocene record of changing uplift rates in southern  
712 Calabria and northeastern Sicily (southern Italy, Central Mediterranean Sea).  
713 *Tectonophysics* 422, 23-40.

714 Antonioli, F., Lo Presti, V., Rovere, A., Ferranti, L., Anzidei, M., Furlani, S.,  
715 Mastronuzzi, G., Orru, P.E., Scicchitano, G., Sannino, G., Spampinato, C.R.,  
716 Pagliarulo, R., Deiana, G., de Sabata, E., Sanso, P., Vacchi, M., Vecchio, A.,  
717 2015. Tidal notches in Mediterranean Sea: a comprehensive analysis. *Quat.*  
718 *Sci. Rev.* 119, 66-84. <https://doi.org/10.1016/j.quascirev.2015.03.016>.

719 Bard, E., Fairbanks, R.G., Hamelin, B., Zindler, A., Hoang, C.T., 1991. Uranium-234  
720 anomalies in corals older than 150,000 years. *Geochim. Cosmochim. Acta* 55,  
721 2385 - 2390.

722 Beydoun, Z.R., As-Saruri, M.L., El-Nakhal, H., Al-Ganad, I.N., Baraba, R.S., Nani, A.O.,  
723 Al-Aawah, M.H., 1998. International lexicon of stratigraphy, Republic of Yemen.  
724 VIII, Asia, fasc, 10b2. 34. IUGS Publ., pp. 1–245.

725 Bird, E.C.F., 2000. Coastal geomorphology: an introduction. Wiley, Chichester, p 322

726 Bosence, D. w. J.; Al-Aawah, M. H.; Davison, I.; Rosen, B. R.; Vita-Finzi C.; Whitaker,  
727 E., 1998. Salt domes and their control on basin margin sedimentation: a case  
728 study from the Tihama Plain, Yemen, in *Sedimentation and Tectonics of Rift*  
729 *Basins: Red Sea-Gulf of Aden* (eds B.H. Purser and D.W.J. Bosence), Chapman &  
730 Hall, London, pp. 448-464.

731 Bosence, D., 2005. A genetic classification of carbonate platforms based on their  
732 basinal and tectonic settings in the Cenozoic. *Sediment Geol.* 175, 49-72.

733 Bosworth W., 2015. Geological evolution of the Red Sea: Historical background,  
734 review, and synthesis. In: Rasul NMA, Stewart ICF (eds) *The Red Sea*. Springer  
735 Earth System Sciences, Springer-Verlag Berlin Heidelberg, pp 45-78.  
736 [https://doi.org/10.1007/978-3-662-45201-1\\_1](https://doi.org/10.1007/978-3-662-45201-1_1).

737 Bosworth, W., 1994. A model for the three-dimensional evolution of continental rift  
738 basins, north-east Africa. In: Schandelmeier, H., Stern, R.J. (Eds.), *Geology of*  
739 *Northeast Africa (Part 2)*, *Geologische Rundschau* 83, pp. 671–688.

740 Brown, G.F., 1970. Eastern margin of the Red Sea and the coastal structures in Saudi  
741 Arabia. *Philos Trans R Soc Lond Ser A, Math Phys Sci* 267:75–87

742 Carbonne, F.; Matteucci, R.; Angelucci, A., 1998. Present-day sedimentation of the  
743 carbonate platforms of the Dahlak Islands, Eritrea, in *Sedimentation and*  
744 *tectonics of rift basins: Red Sea-Gulf of Aden*, (eds B.H. Purser and D.W.J.  
745 Bosence), Chapman & Hall, London, pp. 527-542.

746 Carobene, L., 2015. Marine notches and sea-cave bioerosional grooves in microtidal  
747 areas : examples from the Tyrrhenian and Ligurian coasts-Italy. *J. Coast Res.* 31,  
748 536-556. <https://doi.org/10.2112/JCOASTRES-D-14-00068.1>.

749 Cember, R P, 1989. Bomb Radiocarbon in the Red Sea: A medium-scale gas exchange  
750 experiment. *J. Geophys. Res.* 94(C2), 2111-2123.

751 Chen, J.H., Curran, H.A., White, B., Wasserburg, G.J., 1991. Precise chronology of the  
752 last interglacial period:  $^{234}\text{U}$ - $^{230}\text{Th}$  data from fossil coral reefs in the Bahamas.  
753 *Geol. Soc. Am. Bull.* 103, 82-97.

754 Cheng, H., Edwards, R.L., Shen, C-C., Woodhead, J., Hellstrom, J., Wang, Y.J., Kong,  
755 X.G., Spötl, C., Wang, X.F., Alexander, Jr, E.C., 2013. Improvements in  $^{230}\text{Th}$   
756 dating,  $^{230}\text{Th}$  and  $^{234}\text{U}$  half-life values, and U-Th isotopic measurements by

757 multi-collector inductively coupled plasma mass spectrometry. Earth and  
758 Planet. Sci. Lett., 371–372, 82–91.

759 Cheng, H., Edwards, R.L., Wang, X.F., Woodhead, J., Hellstrom, J., Wang, Y.J., Kong,  
760 X.G., 2008. A new generation of <sup>230</sup>Th dating techniques: tests of precision and  
761 accuracy. *Geochim. Cosmochim. Acta.* 72, 12S.

762 Clark, J.A., Farrell, W.E., Peltier, W.R., 1978. Global changes in post glacial sea-level: a  
763 numerical equation. *Quat. Res.* 9, 265-287.

764 Clifford, M., Horton, C., Schmitz, J., Kantha, L.H., 1997. An oceanographic  
765 nowcast/forecast system for the Red Sea. *J. Geophys. Res. Ocean.* 102, 25101-  
766 25122.

767 Connolly, J.R., 2010. Introduction to x-Ray power diffraction, Springer 2010.  
768 <http://www.ccp14.ac.uk/index.html>.

769 Dabbagh, A.; Hötzl, H., Schnnier, H., 1984. Farasan Islands, In Jado AR, Zoetl JG (eds).  
770 Quaternary period in Saudi Arabia, Volume 2: Springer-Verlag, Vienna, Austria,  
771 pp. 212–220.

772 Davison, I., Al-Kadasi, M., Al-Khribash, S., Al-Subbary, A., Baker, J., Blakey, S.,  
773 Bosence, D., Dart, C., Heaton, R., Heaton, R., McClay, K., Menzies, M., Nichols,  
774 G., Owen, L., Yelland, A., 1994. Geological evolution of the southeastern Red Sea  
775 Rift margin, Republic of Yemen, *Geol. Soc. Am Bull.* 106, 1474-1493.

776 Davison, I., Bosence, D., Alsop, I., Al-Aawah, M.H., 1996. Deformation and  
777 sedimentation around active Miocene salt diapirs on the Tihama Plain,  
778 northwest Yemen, in *Salt Tectonics* (eds I. Alsop, D. Blundell and I. Davison),  
779 *Geol. Soc. Spec. Publ.* 100, pp. 23-39.

780 Defant A (1961) *Physical oceanography*. Pergamon Press, 598 pp

781 Dullo WC, Montaggioni L., 1998. Modern Red Sea coral reefs: a review of their  
782 morphologies and zonation. In: Purser BH, Bosence DWJ (eds) *Sedimentation  
783 and tectonics of rift basins: Red Sea-Gulf of Aden*. Chapman and Hall, London, pp  
784 583-594. [https://doi.org/10.1007/978-94-011-4930-3\\_31](https://doi.org/10.1007/978-94-011-4930-3_31)

785 Edelman-Furstenberg, Y., Scherbacher, M., Hemleben, C. and Almogi-Labin, A., 2001.  
786 Deep-sea benthic foraminifera from the central Red Sea. *J Foramin Res* 31, 48 -  
787 59.

788 Edwards, F. J. 1987. Climate and oceanography. *In*: EDWARDS, F. J. & HEAD, S. M.  
789 (eds) *Red Sea – Key Environments*. Pergamon Press, Oxford, 45-69.

790 Edwards, R.L., Chen, J.H., Ku, T.-L., Wasserburg, G.J., 1987. Precise timing of the last  
791 interglacial period from mass spectrometric analysis of <sup>230</sup>Th in corals. *Science*  
792 236, 1547-1553.

793 El-Asmar, H.M., 1997. Quaternary isotope stratigraphy and paleoclimate of coral reef  
794 terraces, Gulf of Aqaba, south Sinai, Egypt. *Quat. Sci. Rev.* 16, 911-924.

795 El-Nakhal, H., Alaug, A.S., 2013. Nomenclature review of the rock units in the  
796 stratigraphic Lexicon of Yemen. *Iranian Journal of Earth Science* 5, 82-99.

797 Evelpidou, N., Vassilopoulos, A., Pirazzoli, P.A., 2012. Submerged notches on the  
798 coast of Skyros Island (Greece) as evidence for Holocene subsidence.  
799 *Geomorphology*, 141-142, 81-87.

800 Faivre, S., Bakran-Petricioli, T., Horvatincic, N., Sironic, A., 2013. Distinct phases of  
801 relative sea-level changes in the central Adriatic during the last 1500 years-  
802 influence of climatic variations? *Palaeo. Palaeo. Palaeo.* 369, 163 -174.

803 Faure, H., 1975. Recent crustal movements along the Red Sea and Gulf of Aden in  
804 Afar (Ethiopia and T.F.A.I). *Tectonophysics* 29, 479-486.

805 Felis, T., Lohmann, G., Kuhnert, H., Lorenz, S.J., Scholz, D., Patzold, J., Al-Rousan, S.A.,  
806 and Al-Moghrabi, S.M., 2004. Increased seasonality in Middle East  
807 temperatures during the last interglacial period. *Nature* 429, 164-168.

808 Friedman, G. M., 1968. Geology and geochemistry of reefs, carbonate sediments,  
809 and waters, Gulf of Aqaba (Elat), Red Sea. *J. Sediment. Petrol.*, 38, 895-919.

810 Florea, L.J., Vacher, H.L., Donahue, B., Naar, D., 2007. Quaternary cave levels in  
811 peninsular Florida. *Quat. Sci. Rev.* 26, 1344-1361.

812 Friedman, G.M., 1968. Geology and geochemistry of reefs, carbonate sediments, and  
813 waters, Gulf of Aqaba (Elat), Red Sea. *J. Sediment. Petrol.* 38, 895-919.

814 Gallup, C.D., Edwards, R.L., Johnson, R.G., 1994. The timing of high sea levels over  
815 the past 200,000 years. *Science* 263, 796-800.

816 Girdler, R.W., Styles, P., 1974. Two stage Red Sea floor spreading. *Nature* 247, 7-11.

817 Gracia, F.J., Rodriguez-Vidal, Caceres, L.M., Belluomini. G., Benavente, J., Alonso, C.,  
818 2008. Diapiric uplift of an MIS 3 marine deposit in SW Spain: Implications for

819 Late Pleistocene sea level reconstruction and palaeogeography of the Strait of  
820 Gibraltar. *Quat. Sci. Rev.* 27, 2219-2231.

821 Gvartzman, G., 1994. Fluctuations of sea level during the past 400,000 years: The  
822 record of Sinai, Egypt (northern Red Sea). *Coral Reefs* 13, 203–214.  
823 doi:10.1007/BF00303633.

824 Gvartzman, G., Kronfeld, J., Buchbinder, B., 1992. Dated coral reefs of southern Sinai  
825 (Red Sea) and their implication to late Quaternary sea levels. *Mar. Geol.* 108,  
826 29-37.

827 Gvartzman, G., Friedman, G.M., Miller, D.S., 1973. Control and distribution of  
828 uranium in coral reefs during diagenesis. *J Sedim Petrol* 43, 985-997.

829 Hamelin, B., Bard, E., Zindler, A., Fairbanks, R.G., 1991.  $^{234}\text{U}/^{238}\text{U}$  mass spectrometry  
830 of corals: how accurate is the U-Th age of the last interglacial period? *Earth*  
831 *Planet. Sci. Lett.* 106, 169–180.

832 Hearty, P.J., Hollin, J.T., Neumann, A.C., O'leary, M.J., McCulloch, M., O'Leary, M.J.,  
833 2007. Global sea-level fluctuations during the Last Interglaciation (MIS 5e). *Quat.*  
834 *Sci. Rev.* 26, 2090-2112. <https://doi.org/10.1016/j.quascirev.2007.06.019>.

835 Heaton, R.C., Jackson, M.P.A., Bamahmoud, M. and Nani, A.S.O., 1996. Superposed  
836 Neogene extension, contraction, and salt canopy emplacement in the Yemeni  
837 Red Sea, in *Salt Tectonics; A Global Perspective for Exploration* (eds M.P.A.  
838 Jackson, D.G. Roberts and S. Snelson). *Am. Assoc. Petr. Geol. Mem.* 65, pp. 333-  
839 351.

840 Heaton, T. J., Köhler, P., Butzin, M., Bard, E., Reimer, R. W., Austin, W. E. N., Bronk  
841 Ramsey, C., Grootes, P. M., Hughen, K. A., Kromer, B., Reimer, P. J., Adkins, J.,  
842 Burke, A., Cook, M. S., Olsen, J. and Skinner, L. C. 2020. Marine20—The Marine  
843 Radiocarbon Age Calibration Curve (0–55,000 cal BP), *Radiocarbon* 62(4), 779–  
844 820. doi: 10.1017/RDC.2020.68

845 Hein, C.J., FitzGerald, D.M., Milne, G.A., Bard, K., Fattovich, R., 2011. Evolution of a  
846 Pharaonic harbor on the Red Sea: Implication for coastal response to changes in  
847 sea level and climate, *Geology* 39, 687-690. doi: 10.1130/G31928.1

848 Hempton, M.R., 1987. Constraints on Arabian plate motion and extensional history  
849 of the Red Sea. *Tectonics* 6, 687-705.

850 Hibbert, F.D., Rohling, E.J., Dutton, A., Williams, F.H., Chutcharavan, P.M., Zhao, C.,

851 Tamisiea, M.E., 2016. Coral indicators of past sea-level change: a global  
852 repository of U-series dated benchmarks. *Quat. Sci. Rev.* 145, 1-56.  
853 <https://doi.org/10.1016/j.quascirev.2016.04.019>.

854 Hötzl, J.G., 1984. The Red Sea. In: Jado, A.R., Hötzl, J.G. (Eds.), *Quaternary Period in*  
855 *Saudi Arabia*, vol. 2. Springer, Vienna, pp. 13-25.

856 Hötzl, 1984, H., Jado, A.R., Moser, H., Rauert, W. and Zotl, J.G., 1984. The youngest  
857 Pleistocene, In: Jado, A.R., Hötzl, J.G. (Eds.), *Quaternary Period in Saudi Arabia*,  
858 vol. 2., Springer, Vienna, pp. 314-324.

859 Jaffey, A.H., Flynn, K.F., Glendenin, L.E., Bentley, W.C., Essling, A.M., 1971. Precision  
860 measurement of half-lives and specific activities of  $^{235}\text{U}$  and  $^{238}\text{U}$ . *Phys. Rev. C* 4,  
861 1889 -1906.

862 Kelletat, D., Scheffers, A., 2005. Ergänzende Informationen zum Sumatra-Andaman-  
863 Tsunami vom 26.12.2004. *Geographische Rundschau* 57 (9): 64-65.

864 Kelsey, H.M., 1990. Late Quaternary deformation of marine terraces on the Cascadia  
865 subduction zone near Cape Blanco, Oregon. *Tectonics* 9, 983–1014.

866 Kelsey, H.M., and Bockheim, J.G., 1994. Coastal landscape evolution as a function of  
867 eustasy and surface uplift rate, Cascadia margin, southern Oregon. *Geol. Soc.*  
868 *Am. Bull.* 106, 840–854.

869 Kershaw, S., Guo, L., 2001. Marine notches in coastal cliffs: indicators of relative sea-  
870 level change, Perachors Peninsula, central Greece, *Marine Geology* 179, 213-228.

871 Lambeck, K., Purcell, A., Dutton, A., 2012. The anatomy of interglacial sea-levels: The  
872 relationship between sea-levels and ice volumes during the Last Interglacial.  
873 *Earth Planet. Sci. Lett.* 4-11, 351-316. doi:10.1016/j.epsl.2011.08.026.

874 Lambeck, K., Purcell, A., Flemming, N.C., Vita-Finzi, C., Alsharekh, A.M., Bailey, G.N.,  
875 2011. Sea level and shoreline reconstructions for the Red Sea: isostatic and  
876 tectonic considerations and implications for hominin migration out of Africa.  
877 *Quat. Sci. Rev.* 30, 3542-3574.  
878 <http://dx.doi.org/10.1016/j.quascirev.2011.08.008>.

879 Lambeck, K., Rouby, H., Purcell, A., Sun, Y., Sambridge, M., 2014. Sea level and  
880 global ice volumes from the Last Glacial Maximum to the Holocene. *Proc. Natl.*  
881 *Acad. Sci. U.S.A.* 111(43), 15296-15303, doi:10.1073/pnas.1411762111.

882 Lamy, F., Arz, H.W., Bond, G.C., Bahr, A. and Patzold, J., 2006. Multicentennial-scale  
883 hydrological change in the Black Sea and northern Red Sea during the Holocene  
884 and the Arctic/North Atlantic Oscillation, *Paleoceanography* 21, 1-11.  
885 doi:10.1029/2005PA001184

886 Langodan, S., Cavaleri, L., Pomaro, A., Portilla, J., AbuAlNaja, Y., Hoteit, I., 2018.  
887 Unraveling climatic wind and wave trends in the Red Sea using wave spectra  
888 partitioning: *J. of Climate*. 31, 1881-1895. DOI: [10.1175/JCLI-D-17-0295.1](https://doi.org/10.1175/JCLI-D-17-0295.1)

889 Langodan S., Cavaleri, L., Pomaro, A., Viswanadhapalli, Y, Bertotti L. Hoteit, I., 2017.  
890 The climatology of the Red Sea-part 2: the waves. *Int. J. Climat.* DOI:  
891 [10.1002/joc.5101](https://doi.org/10.1002/joc.5101).

892 Long, A., 2001. Mid-Holocene sea-level change and coastal evolution. *Prog. Phys.*  
893 *Geogr.* 25, 399 - 408.

894 Lorscheid, T., Stocchi, P., Casella, E., Gomez-Pujol, L., Vacchi, M., Mann, T., Rovere,  
895 A., 2017. Paleo sea-level changes and relative sea-level indicators: precise  
896 measurements, indicative meaning and glacial isostatic adjustment perspectives  
897 from Mallorca (Western Mediterranean). *Palaeogeogr. Palaeoclimatol.*  
898 *Palaeoecol.* 473, 94-107. <https://doi.org/10.1016/j.palaeo.2017.02.028>.

899 May, V.J., Heeps, C., 1985. The Nature and Rates of Change on Chalk  
900 coastlines. *Zeitschrift für Geomorphologie NF Suppl. Band 57*, 81-94.

901 Milne, G.A., Gehrels, W.R., Hughes, C.W., Tamisiea, M.E., 2009. Identifying the  
902 causes of sea-level change. *Nat. Geosci.* 2, 471-478.

903 Milne G. A., Mitrovica J. X., 2008. Searching for eustasy in deglacial sea level  
904 histories. *Quat Sci Rev.* 27, 2292-2302. doi:10.1016/j.quascirev.2008.08.018.

905 Mitchell, D.J.W., Allen, R.B., Salama, W., Abduzakm, A., 1992. Tectonostratigraphic  
906 framework and hydrocarbon potential of the Red Sea. *J Petrol. Geol.* 15 (2),  
907 187-210

908 Mitrovica, J.X., Milne, G.A., 2002. On the origin of late Holocene sea-level highstands  
909 within equatorial ocean basins. *Quat. Sci. Rev.* 21, 2179-2190.  
910 doi:10.1016/S0277-3791(02)00080-X.

911 Mitrovica, J.X., Peltier, W.R., 1991. On postglacial geoid subsidence over the  
912 equatorial oceans. *J. Geophys. Res.* 96 (B12), 20053-20071.

913 Moses, C.A., 2013. Tropical rock coasts: Cliff, notch and Platform erosion dynamics,

914 Progress in Physical Geography 37, 206-226. DOI: 10.1177/0309133312460073

915 Moustafa, Y.A., Patzold, J., Loya, Y., Wefer, G., 2000. Mid-Holocene stable isotope

916 record of corals from the northern Red Sea, International Journal of Earth

917 Sciences 88, 742–751, 2000.

918 Nakada, M., Lambeck, K., 1987. Glacial rebound and relative sea-level variations: a

919 new appraisal. Geoph. J. R. Astron. Soc. 90, 171-224.

920 Neumann, A.C., Hearty, P.J., 1996. Rapid sea-level changes at the close of the last

921 interglacial (substage 5e) recorded in Bahamian island geology. Geology 24, 775-

922 778.

923 Pedoja, K., Husson, L., Johnson, M.E., Melnick, D., Witt, C., Pochat, S. et al., 2014.

924 Coastal staircase sequence reflecting sea-level oscillations and tectonic uplift

925 during the Quaternary and Neogene. Earth-Sci. Rev. 132, 13-38.

926 Phillips, B.A.M., 1970. The significance of inheritance in the interpretation of marine

927 and lacustrine coastal histories. Lakehead University Review 3, 36–45.

928 Pirazzoli, P.A., Evelpidou, N., 2013. Tidal notches: a sea-level indicator of uncertain

929 archival trustworthiness. Palaeogeogr. Palaeoclimatol. Palaeoecol. 369, 377-384.

930 Pirazzoli, P.A., Stiros, S.C., Arnold, M., Laborel, J., Laborel-Deguen, F., Papageorgiou,

931 S., 1994a. Episodic uplift deduced from Holocene shorelines in the Perachora

932 Peninsula, Corinth area, Greece. Tectonophysics 229, 201–209.

933 Pirazzoli, P.A., Stiros, S.C., Laborel, J., Laborel-Deguen, F., Arnold, M., Papageorgiou,

934 S., Morhange, C., 1994b. Late-Holocene shoreline changes related to

935 palaeoseismic events in the Ionian Islands, Greece. *The Holocene* 4, 397–405.

936 Pirazzoli, P.A., Pluet, J., 1991. World atlas of Holocene sea-level changes. Elsevier

937 Oceanogr. Ser. 58, 299

938 Pirazzoli, P.A., 1986. Marine notches. In: van de Plassche, O. (Ed.), Sea-level

939 Research: a Manual for the Collection and Evaluation of Data. Geo Books,

940 Norwich, pp. 361-400.

941 Plaziat, J.-C., Baltzer, F., Chouki, A., Conchon, O., Freytet, P., Orszag-Sperber, F.,

942 Raguideau, A., Reyss, J.-L., 1998. Quaternary marine and continental

943 sedimentation in the northern Red Sea and Gulf of Suez (Egyptian coast):

944 influences of rift tectonics, climatic changes and sea-level fluctuations. In:

945 Purser, B.H., Bosence, D.W.J. (Eds.), Sedimentation and Tectonics in Rift Basins:

946 Red Sea—Gulf of Aden. Chapman and Hall, London, pp. 537–573.

947 Plaziat J.-C., Baltzer F., Choukri A., Conchon O., Freytet P., Orszag-Sperber F., Purser  
948 B.H., Raguideau A., Reyss J.-L., 1995. Quaternary changes in the Egyptian shore-  
949 line of the northwestern Red Sea and Gulf of Suez. *Quaternary International*,  
950 Amsterdam 29-30, 11-22.

951 Purkis S.J., Harris P.M., Ellis J., 2012. Patterns of sedimentation in the contemporary  
952 Red Sea as an analog for ancient carbonates in rift settings. *J. Sediment. Res.* 82,  
953 859-870.

954 Purkis, S.J., Riegl, B.M., 2012. Geomorphology and reef building in the SE Gulf. In:  
955 Coral reefs of the Gulf: adaptation to climatic extremes hardcover. Springer,  
956 Netherlands. ISBN 978-94-007-3007-6

957 Purser, B.H., Hötzl, H., 1988. The sedimentary evolution of the Red Sea rift: a  
958 comparison of the northwest (Egyptian) and northeast (Saudi Arabian) margins.  
959 *Tectonophysics*, 153, 193-208.

960 Ralston, D.K., Jiang, H., Ferrar, T.F., 2013. Waves in Red Sea: Response to monsoonal  
961 and mountain gap winds. *Cont. Shelf Res.* 65, 1–13.  
962 <https://doi.org/10.1016/j.csr.2013.05.017>.

963 Reimer, P.J., Reimer, R.W., 2020. Marine reservoir correction database.  
964 <http://calib.org/marine/> (accessed 12<sup>th</sup> Oct 2020).

965 Rodriguez-Vidal, J., Caceres, L.M., Abad, M., Ruiz, F., Martinez-Aguirre, A. 2007.  
966 Morphosedimentary evidence of the Last Interglacial Maximum on the coast of  
967 Governor’s Beach, Gibraltar, *Geogaceta* 42, 107-110.

968 Rovere, A., Hearty, P.J., Austermann, J., Mitrovica, J.X., Gale, J., Moucha, R., Forte,  
969 A.M., Raymo, M.E., 2015. Mid-Pliocene shorelines of the US Atlantic Coastal  
970 Plain - An improved elevation database with comparison to Earth model  
971 predictions. *Earth-Sci. Rev.* 145, 117-131.

972 Rovere, A., Raymo, M.E., Vacchi, M., Lorscheid, T., Stocchi, P., Gómez-Pujol, L., Harris,  
973 D.L., Casella, E., O’Leary, M.J., Hearty, P.J., 2016. The analysis of Last Interglacial  
974 (MIS 5e) relative sea-level indicators: Reconstructing sea-level in a warmer  
975 world. *Earth-Science Reviews* 159, 404-427.  
976 <https://doi.org/10.1016/j.earscirev.2016.06.006>.

977 Rowlands, G. and Purkis, S., 2015. Geomorphology of shallow water coral reef  
978 environments in the Red Sea. In: Rasul N. M. A. and Stewart I. C. F (eds.), the Red  
979 Sea, Springer Earth System Sciences, springer-Verlag Berlin Heidelberg.

980 Rowlands, G. P., Purkis S.J., Bruckner, A.W., 2014. Diversity in the geomorphology of  
981 shallow-water carbonate depositional systems in the Saudi Arabian Red Sea.  
982 Geomorphology. doi:10.1016/j. geomorph.2014.03.014

983 Rust, R., Kershaw, S., 2000. Holocene tectonic uplift patterns in northeastern Sicily:  
984 evidence from marine notches in coastal outcrops. *Mar. Geol.* 167 (1-2), 105-  
985 126.

986 Schneiderwind, S., Boulton, S.J., Papanikolaou, I., Kázmér, M., Reicherter, K., 2017.  
987 Numerical modeling of tidal notch sequences on rocky coasts of the  
988 Mediterranean Basin. *J. Geophys. Res. Earth Surf.* 122, 1154–1181.  
989 doi:10.1002/2016JF004132.

990 Scholz, D., Mangini, A., Felis, T., 2004. U-series dating of diagenetically altered fossil  
991 reef corals. *Earth Planet. Sci. Lett.* 218, 163–178.

992 Shaked, Y., Lazar, B., Marco, S., Stein, M., Tchernov, D., Agnon, A., 2005. Evolution of  
993 fringing reefs: space and time constraints from the Gulf of Aqaba. *Coral Reefs*  
994 24. 165-172, DOI 10.1007/s00338-004-0454-2.

995 Shaked, Y., Agnon, A., Lazar, B., Marco, S., Avner, U., Stein, M., 2004. Large  
996 earthquakes kill coral reefs at the north-west Gulf of Aqaba. *Terra Nova* 16, 133–  
997 138.

998 Shaked, Y., Marco, S., Lazar, B., Stein, M., Cohen, C., Sass, E., Agnon, A., 2002. Late  
999 Holocene shorelines at the Gulf of Aqaba: migrating shorelines under conditions  
1000 of tectonic and sea level stability. In: EGU Stephan Mueller Special Publication  
1001 Series, vol. 2 105-111.

1002 Shanas, P.R., Aboobacker, V.M., Albarakati, A.M.A., Zubier, K.M., 2017. Climate  
1003 driven variability of wind in the Red Sea, *Ocean Modelling* 119, 105-117.  
1004 <http://dx.doi.org/10.1016/j.ocemod.2017.10.001>.

1005 Shen, C.-C., Edwards, R.L., Cheng, H., Dorale, J.A., Thomas, R.B., Moran, S.B.,  
1006 Weinstein, S., Edmonds, H.N., 2002. Uranium and thorium isotopic and  
1007 concentration measurements by magnetic sector inductively coupled plasma  
1008 mass spectrometry. *Chem. Geol.* 185, 165-178.

1009 Sofianos, S.S., Johns, W.E., 2003. An oceanic general circulation model (OGCM)  
1010 investigation of the Red Sea circulation: 2. Three-dimensional circulation in the  
1011 Red Sea. *J. Geophys. Res.* 108 (C3), 3066.

1012 Stattegger, K., Tjallingii, R., Saito, Y., Michelli, M., Thanh, N.T., Wetzel, A., 2013. Mid  
1013 to late Holocene sea-level reconstruction of Southeast Vietnam using beachrock  
1014 and beach-ridge deposits, *Global Planet Change* 110, 214-222.  
1015 <http://dx.doi.org/10.1016/j.gloplacha.2013.08.014>.

1016 Stirling, C.H., Andersen, M.B., 2009. Uranium-series dating of fossil coral reefs:  
1017 extending the sea-level record beyond the last glacial cycle. *Earth Planet. Sci.*  
1018 *Lett.* 284, 269-283. <https://doi.org/10.1016/j.epsl.2009.04.045>.

1019 Stiros S.C., Pirazzoli, P.A., Fontugne, M., 2009. New evidence of Holocene coastal  
1020 uplift in the Strophades Islets (W Hellenic Arc, Greece). *Mar. Geol.*, 267, 207-  
1021 211.

1022 Strasser, A. and Strohmenger, C., 1997. Early diagenesis in Pleistocene coral reefs,  
1023 southern Sinai, Egypt: response to tectonics, sea-level and climate,  
1024 *Sedimentology* 44, 537-558.

1025 Trenhaile, A.S., 2015. Coastal notches: their morphology, formation, and function.  
1026 *Earth-Science Reviews* 150, 285-304.

1027 Trenhaile, A.S., Pepper, D.A., Trenhaile, R.W., Dalimonte, M., 1998. Stacks and  
1028 notches at Hopewell Rocks, New Brunswick, *Canada. Earth Surf. Process. Land.*  
1029 23, 975–988.

1030 Trenhaile, A.S., 1987. *The Geomorphology of Rock Coasts*. Oxford University Press,  
1031 Oxford.

1032 Trenhaile, A.S., 1972. The shore platforms of the Vale of Glamorgan, Wales. *Trans.*  
1033 *Inst. Br. Geogr.* 56, 127-144.

1034 Woodroffe, C.D. and Webster, J.M., 2014. Coral reefs and sea-level change, *Mar.*  
1035 *Geol.* 352, 248-267.

1036 Wright V.P., 1994. Paleosols in shallow marine carbonate sequences, *Earth Science*  
1037 *Reviews* 35, 367-395.

1038 Yokoyama, Y., Esat, T. M., Lambeck, K., 2001. Last Glacial sea-level change deduced  
1039 from uplifted coral terraces of Huon Peninsula, Papua New Guinea. *Quatern Int.*  
1040 83-85:275–283.

- 1041 Youssef, El. A., 1991. A note on the geomorphology of the coastal plain between Al  
1042 Hudaydah and Al Salif Peninsula, Red Sea Coast, Yemen Arab Republic. The  
1043 Geogr. J. 157, 71-73.
- 1044 Yu, K.-F., Zhao, J.-X., 2010. U-series dates of Great Barrier Reef corals suggest at least  
1045 + 0.7 m sea level ~7000 years ago. The Holocene 20, 161–168.